Sister Rod Destructive Examinations (FY21)

Appendix E: Mechanical Testing

Spent Fuel and Waste Disposition

Prepared for
US Department of Energy

Spent Fuel and Waste Science and Technology

Oak Ridge National Laboratory
Rose Montgomery, Darren Skitt, Muhammet Ayanoglu
Yong Yan, Ben Garrison

March 31, 2022

M2SF-22OR010201042

ORNL/SPR-2021/2307

ORNL/SPR-2020/1790 Revision 1

SUMMARY

This report documents work performed under the Spent Fuel and Waste Disposition's Spent Fuel and Waste Science and Technology program for the US Department of Energy (DOE) Office of Nuclear Energy (NE). This work was performed to fulfill Level 2 Milestone M2SF-22OR010201042, "FY2021 ORNL Report on High Burnup Sibling Pin Testing Results," within work package SF-22OR01020104 and is an update to the work reported in M2SF-21OR010201032, M2SF-19ORO010201026 and M2SF-19OR010201028.

As a part of the DOE NE High Burnup Spent Fuel Data Project, Oak Ridge National Laboratory (ORNL) is performing destructive examinations (DEs) of high burnup (HBU) (>45 GWd/MTU) spent nuclear fuel (SNF) rods from the North Anna Nuclear Power Station operated by Dominion Energy. The SNF rods, called *sister rods* or *sibling rods*, are all HBU and include four different kinds of fuel rod cladding: standard Zircaloy-4 (Zirc-4), low-tin Zirc-4, ZIRLO, and M5. The DEs are being conducted to obtain a baseline of the HBU rod's condition before dry storage and are focused on understanding overall SNF rod strength and durability. Composite fuel and defueled cladding will be tested to derive material properties. Although the data generated can be used for multiple purposes, one primary goal for obtaining the post-irradiation examination data and the associated measured mechanical properties is to support SNF dry storage licensing and relicensing activities by (1) addressing identified knowledge gaps and (2) enhancing the technical basis for post-storage transportation, handling, and subsequent disposition.

This report documents the status of the ORNL Phase 1 DE activities related to the mechanical testing of selected sister rods in Phase 1 of the sister rod test program.

Table ES-1 summarizes the mechanical test status.

Table ES-1. DE status.

Planned DE		Status	Comments
DE.07	Conduct four-point bend (4PB) tests	In progress	All Phase 1 tests are complete except for those planned for aerosol collection. Tests were conducted at room temperature (RT) and at 200°C. Data evaluation is in progress. The flexural strength and strain at fracture, 0.2% offset yield strength, and flexural modulus were calculated for the tests completed. Generally, the heat-treated M5 and ZIRLO-clad specimens have higher ductility than the baseline specimens. The mass loss from the specimen resulting from fracture was measured during the 4PB tests. There was no trend of pellet mass loss related to test temperature, although the RT fractures seemed more energetic than the 200°C fracture. Each pellet weighed approximately 5.1–7.0 g, so the maximum mass released from the cladding represents about ¼ of a pellet, whereas the more typical 0.4 g mass released is less than ⅒ of a full pellet. The uncertainty of the 4PB test in ORNL's configuration was calculated and integrated with the results. In the process of calculating the uncertainties, errors in the stress and strain

Planned DE		Status	Comments
			calculation results tabulated in the 11/30/2020 report were found and corrected.
DE.08	Conduct axial tensile tests	In progress	ORNL tested a specimen available from a previous program (M5 clad pressurized water reactor [PWR] rod). Four trials were performed, and the specimen broke every time at the clamp on the upper axial tension jaws. This indicates a sensitivity of the cladding and is consistent with Pacific Northwest National Laboratory's (PNNL's) experience. An alternative method to clamp the specimens in the load frame is being investigated.
DE.09	Test for American Society for Testing and Materials (ASTM) microhardness	Not started	In FY21, microhardness tests were performed on one defueled polished sample prepared from segment F35P17-2735-2754 (heat-treated Zirc-4 cladding). Each quadrant of the cladding (Quad A, B, C, D) was indented across its thickness, and a fifth test was performed at a location where extensive waterside oxide spalling occurred (Quad AB). The measured HV increased from cladding ID to OD across the cladding thickness and ranged from 251± 9 to 298± 11 HV. The oxide layer was found to be significantly harder than the base cladding, at an average measured HV of 947 ± 67. The results are consistent with those from PNNL.
DE.10	Conduct fueled ring compression tests (RCTs)	Complete	Fueled RCTs are complete. There is no appreciable difference in the maximum load-bearing capability of the segments from RT to 200°C. Cladding type also does not greatly influence the load-bearing capability, and there does not appear to be a difference related to the heat-treatment applied to some of the rods. The main observed variant is the orientation of the major cracks in the pellet because these appear to nucleate fracture of the adjacent cladding and determine the pellet fracture plane. The observed transverse bearing load of the specimen is 16.4 kN (3,690 lb_f) on average, with a minimum load-bearing capability of 12.3 kN (2,766 lb_f) for the tested segments.
DE.14	Perform burst tests	Experiment design in progress	Existing equipment at the Irradiated Fuels Examination Laboratory (IFEL) is not capable of achieving the pressures needed at the proposed test temperatures. ORNL is collaborating with PNNL to design a new system to pressurize segments for burst that is similar to their system for cladding burst, with the exception that ORNL will use a gas. With a basic design in hand, ORNL plans to acquire the necessary equipment in FY22.

ACKNOWLEDGMENTS

Many thanks to our US Department of Energy Office of Nuclear Energy sponsor Ned Larson, along with the Spent Fuel and Waste Science and Technology storage and transportation program leadership for their continued support. The sister rod project would not have been possible without the vision and support of the Electric Power Research Institute, Westinghouse, Framatome, and Dominion Energy.

This work would not have been possible without the support and expertise provided by the leadership and staff members of the ORNL's Irradiated Fuel Examination Laboratory. Special thanks go to Jerid Metcalf, Scott Thurman, John Hinds, and Brian Woody for their assistance with in-cell testing activities. Rick Henry has the unenviable task of tracking the bits and pieces of sister rods and their moves around the hot cell and to other facilities, and we very much appreciate his patience and continued support. Jim Miller, Mark Delph, and Russ Smith have been vital in supporting the deployment of new equipment to the cell, and we appreciate their continued support.

This page is intentionally left blank.

CONTENTS

This page is intentionally left blank.

LIST OF FIGURES

LIST OF TABLES

This page is intentionally left blank.

REVISION HISTORY

Date	Changes
10/29/2020	This appendix contains new information on the mechanical testing results.
11/30/2020	Comments received on the 10/29/2020 draft were incorporated, and the document numbering was revised to reflect its M2 status.
10/29/2021	The appendix has been revised to incorporate new data (Section E-4) and to correct calculated results of the 4PB tests (modified Table E-2 and Figs. E-10 through E-13, added Fig. E-14). Minor changes in the text were made in Sections E-3, E-6, E-2.6, and E-2.4. The summary has been updated.
3/31/2022	Comments received on the 10/29/2021 draft were incorporated, the document number was revised to reflect its M2 status, and the document date was changed. More information was added in section 2.1.4 relative to the use of elastic beam theory in the four point bend data reduction.

This page is intentionally left blank.

ACRONYMS

4PB	four-point bend
ANL	Argonne National Laboratory
ASTM	American Society for Testing and Materials
CIRFT	cyclic integrated reversible-bending fatigue tester
DE	destructive examination
DOE	US Department of Energy
EI	flexural rigidity
FHT	full-length fuel rod heat treatment
HBU	high burnup
HV	Vickers hardness
IFEL	Irradiated Fuels Examination Laboratory
LAMDA	Low Activation Materials Development and Analysis
LT	low tin
MET	metallography
NDE	nondestructive examination
NE	Office of Nuclear Energy
ORNL	Oak Ridge National Laboratory
PNNL	Pacific Northwest National Laboratory
PWR	pressurized water reactor
RCT	ring compression test
RT	room temperature
SNF	spent nuclear fuel

This page is intentionally left blank.

E-1. Mechanical Test Frame Installation

As a part of the US Department of Energy (DOE) Office of Nuclear Energy (NE) High Burnup Spent Fuel Data Project [E-1], Oak Ridge National Laboratory (ORNL) is performing destructive examinations (DEs) of high burnup (HBU) (>45 GWd/MTU) spent nuclear fuel (SNF) rods from the North Anna Nuclear Power Station operated by Dominion Energy. The SNF rods, called *sister rods* or *sibling rods*, are all HBU and include four different kinds of fuel rod cladding: standard Zircaloy-4 (Zirc-4), low-tin (LT) Zirc-4, ZIRLO, and M5. The Phase 1 DEs [E-2, E-3] are being conducted to obtain a baseline of the HBU rod's condition before dry storage and are focused on understanding overall SNF rod strength and durability. Composite fuel and defueled cladding will be tested to derive material properties. Although the data generated can be used for multiple purposes, one primary goal for obtaining the postirradiation examination data and the associated measured mechanical properties is to support SNF dry storage licensing and relicensing activities by (1) addressing identified knowledge gaps and (2) enhancing the technical basis for post-storage transportation, handling, and subsequent disposition.

To provide the capability for mechanical testing, a large Instron load frame (65 × 31 × 29 in.) with a 30 kN capacity (~1 ton of loading force) was installed in the Irradiated Fuels Examination Facility (IFEL) north hot cell. The cell location was selected based on its accessibility and its lower dose rates (~150 R/h).

During FY20, the load frame was modified for durability in the radiation field and to provide remote manipulation capabilities. Lead shielding was placed around the load frame's instrumentation string to provide more protection from radiation damage.

The load frame was successfully installed in the cell in June 2020. It was carefully rigged, lifted, and transported to the hot cell loading bay (Figure E-1, left) where it was placed on a forklift. The rigging was left in place for in-cell handling. The load frame was moved to the hot cell charging area and was then moved into the cell using the primary airlock (Figure E-1, right). From there, the in-cell crane used the same rigging to lift the load frame and move it to the north cell operating position, as shown in Figure E-2 (left). Standard bubble levels were used to check the level and plumb of the installed load frame.

To connect the control unit in the operating area of the hot cell with the load frame in the cell, instrumentation and power cabling were run through the cell's 3 ft thick wall using a service plug. As shown in Figure E-2 (right), this required removing the existing plug—which momentarily left an open path from the hot cell interior to the operating area—and then replacing it with the new plug. All cables were preinstalled in the service plug, and it was sealed before the evolution. The challenge was to install the heavy lead-shielded service plug without damaging the cables.

After the load frame was installed in the hot cell, it was cycled through several tests using surrogate materials to verify its operation.

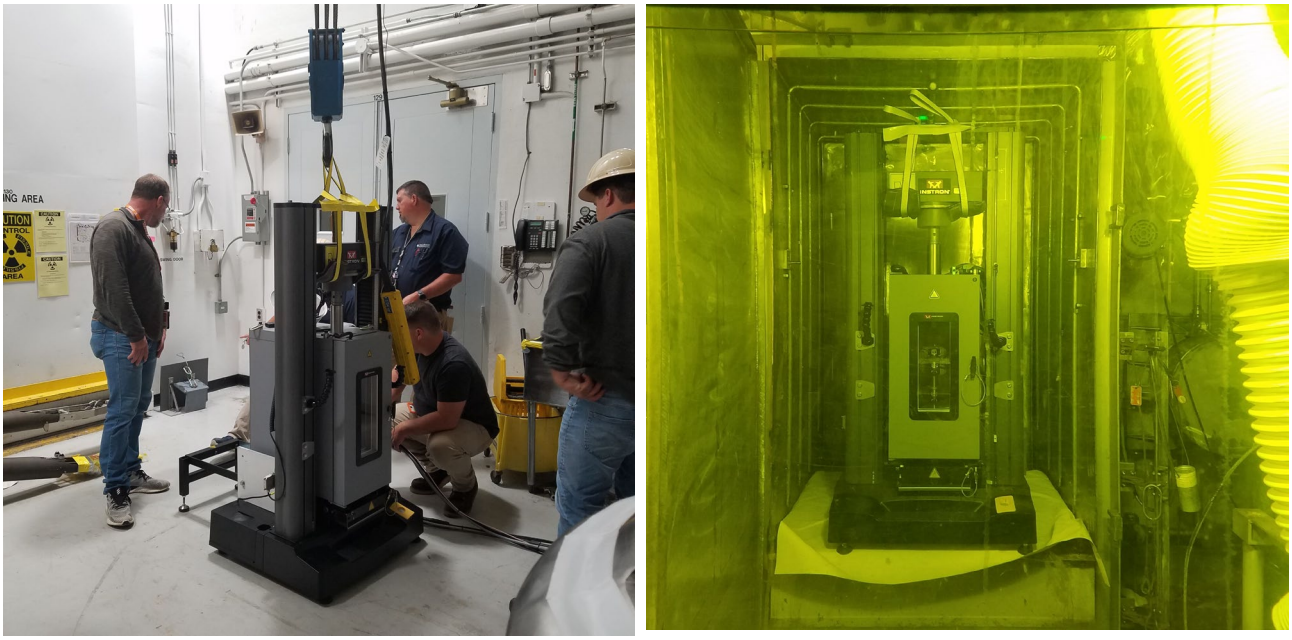

Figure E-1. The Instron load frame and furnace were moved to the hot cell loading bay (left) and into the hot cell through the cell's primary airlock (right).

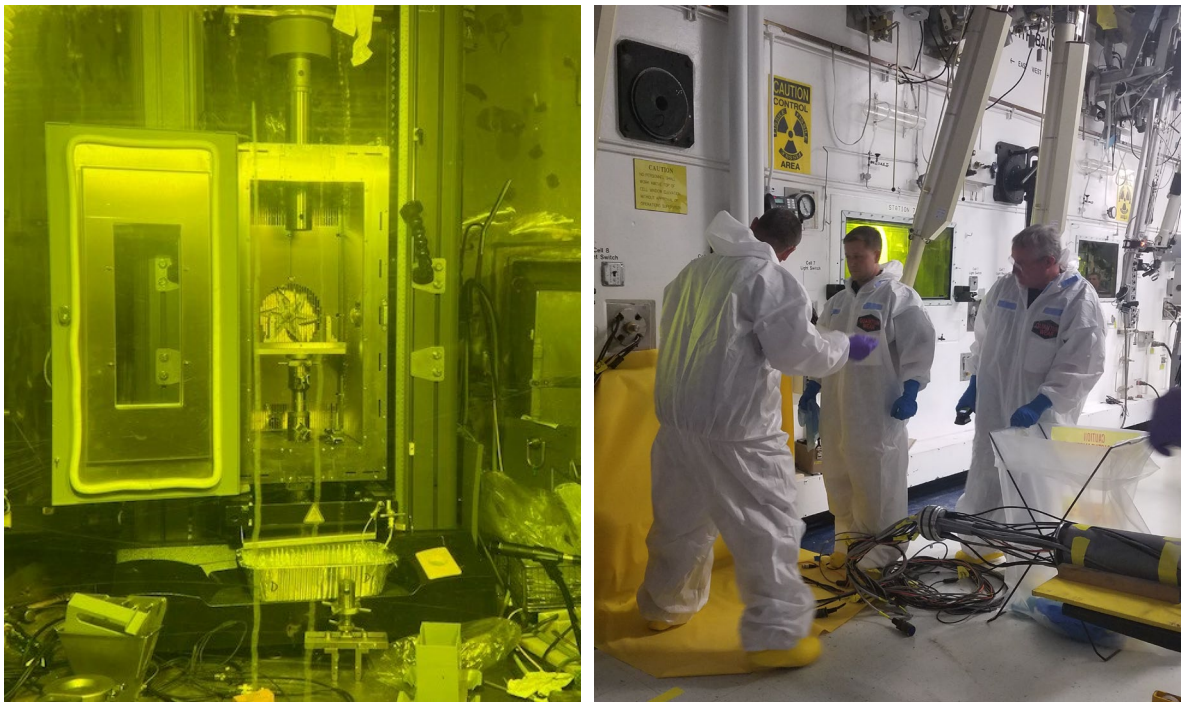

Figure E-2. The Instron load frame and furnace were placed in the north hot cell (left), and the service plug containing all instrumentation and power was installed (right).

E-2. Four-Point Bend Tests

The four-point bend (4PB) test provides values for the modulus of elasticity in bending (the *flexural modulus*), as well as the flexural stress and flexural strain response. It is traditionally the test used to study brittle materials in which the number and severity of flaws exposed to the maximum stress is directly related to the flexural strength and crack initiation.

ORNL is testing fuel rod segments with pellets (termed a "composite rod) and PNNL is testing the defueled cladding. The composite rod's performance is different from the empty cladding's performance. The presence of the pellets is expected to provide stiffening and support to the cladding, but the discontinuities inherent in the pellets also locally increase stress in the cladding. Therefore, the results of the ORNL composite rod tests can be compared with the PNNL defueled cladding tests to provide an indication of the overall strength of the composite rod and the inherent effect of the pellets, but the composite rod test results should not be construed as cladding properties.

Several ASTM standards are available for 4PB, including *Standard Test Method for Flexural Strength of Advanced Ceramics at Ambient Temperature*[E-4] and *Standard Test Methods for Flexural Properties of Polymer Matrix Composite Materials* [E-5], which were used to guide selection of the fixture geometry and test gauge length. There is not a specific ASTM test method to measure the flexural properties of SNF rods, but ASTM C1161 [E-4] and ASTM D7264/D7264M [E-5] provide guidance and information used to inform the approach used to test the spent fuel rod segments. The ASTM guidelines for these tests typically call for rectangular specimens, while the shape of the fuel rods tested can be generalized as cylindrical. ASTM C1161 discusses the use of a four-point bend test on single-material ceramic coupons and ASTM D7264/D7264M addresses testing of multi-material coupons such as fiber-reinforced polymers. The fuel rod segments being tested are composites consisting of multiple pellets within a cladding, and as discussed by ASTM D7264/D7264M, no composite material is perfectly symmetric. Additionally, the pelleted rods contain many discontinuities that can affect local stress, such as the end features on the pellets (chamfers and dishes), cracks in the pellets developed during reactor operation, bonded areas between the pellets and the cladding, and cladding precipitated hydrides.

Room temperature (RT) and 200°C tests were completed. The list of specimens is provided in Table E-1. Video and audio records of the tests were acquired, along with the displacement and load results. Each test segment was weighed before testing. A tray was placed below the specimen to catch debris, and the broken segments and debris were weighed after each test.

Several 4PB tests will be completed with the aerosol collection system to better quantify the size distribution and quantity of aerosol particles released during fracture. The aerosol tests have not yet been completed, as discussed in Appendix I.

The load frame and associated test fixturing (shown in Figure E-3) applies load at four points on the fuel rod specimen. The upper fixture is advanced at a selected fixed displacement rate in the downward direction, whereas the lower fixture is fixed and does not move. The fixture used is standard off-the-shelf equipment for 4PB, except that wire stops were added to ensure that the rod would not roll off the back of the fixture before the test could start. For tests at temperature, the load frame's furnace is pulled forward. The specimen is placed on the fixture, and the two are heated simultaneously to the test temperature. The stock furnace thermocouple was used to measure chamber temperature, and a minimum 15 minutes of hold time at temperature was allotted to let the fixture and specimen reach steady state. ASTM C1161–18 [E-4] and ASTM D7264/D7264M–15 [E-5] were used in setting up and evaluating the test data. ASTM E8/E8M–16a [E-6] was used in evaluating the 0.2% offset yield strength.

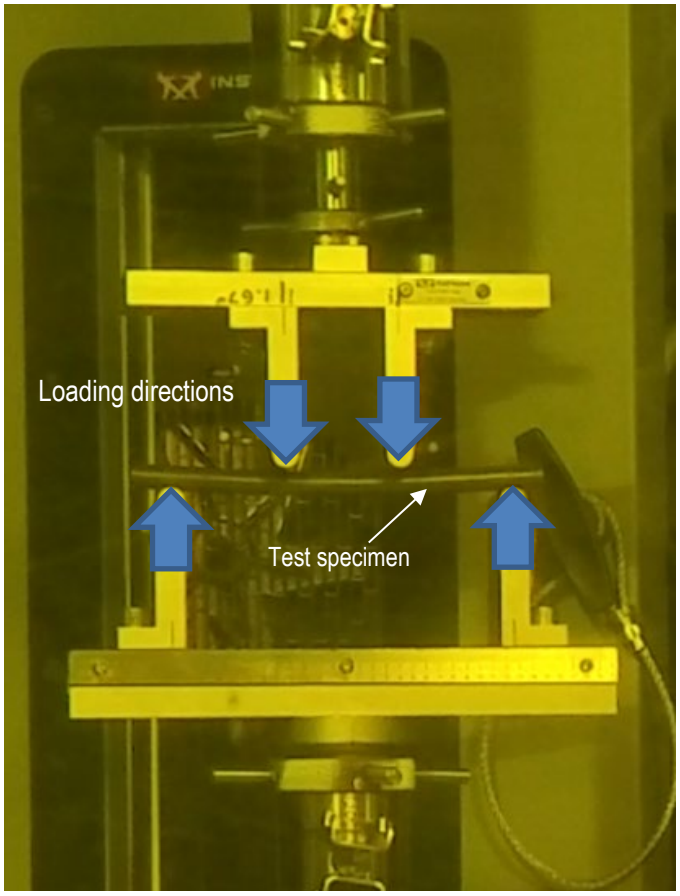

Figure E-3. The load frame configured for 4PB tests of a sister rod specimen.

Table E-1. List of specimens for 4PB.

Specimen ID#			Cladding alloy	Test temp. (°C)	Specimen heat treatment before test	In-reactor operating zone	Specimen average burnup (GWd/MTU)	Specimen average oxide thickness (μ)	Test status
30AD05	850	1003	M5	200	None	zone1	60	3	Complete
30AD05	1003	1156	M5	RT	None	zone1	60	3	Future test with aerosol collection
30AD05	1299	1452	M5	RT	None	zone1	60	4	Complete
30AD05	1800	1953	M5	200	None	zone1	59	4	Complete
30AE14	825	978	M5	200	FHT*	zone1	58	4	Complete
30AE14	978	1131	M5	RT	FHT	zone1	59	4	Complete
30AE14	1800	1953	M5	RT	FHT	zone1	60	9	Future test with aerosol collection
30AE14	2050	2203	M5	200	FHT	zone1	60	10	Complete
3D8E14	872	1025	ZIRLO	200	None	zone1	64	10	Complete
3D8E14	1025	1178	ZIRLO	RT	None	zone1	64	11	Complete
3D8E14	1907	2060	ZIRLO	200	None	zone1	64	21	Complete
3D8E14	2810	2963	ZIRLO	RT	None	zone1	63	41	Complete
3F9N05	872	1025	ZIRLO	200	FHT	zone1	59	10	Complete
3F9N05	1910	2063	ZIRLO	200	FHT	zone1	59	23	complete
3F9N05	2063	2216	ZIRLO	RT	FHT	zone1	59	28	Complete
3F9N05	2882	3035	ZIRLO	RT	FHT	zone1	58	46	Future test with aerosol collection
3A1F05	1279	1432	LT Zirc-4	RT	None	zone1	57	23	Complete
3A1F05	1432	1585	LT Zirc-4	200	None	zone1	56	34	Complete
3A1F05	2230	2383	LT Zirc-4	200	None	grid4	54	72	Complete
3A1F05	2402	2555	LT Zirc-4	RT	None	zone1	55	117	Future test with aerosol collection
F35P17	1319	1472	Zirc-4	RT	FHT	zone1	52	26	Complete
F35P17	1472	1625	Zirc-4	200	FHT	zone1	53	37	Complete
F35P17	2230	2383	Zirc-4	200	FHT	grid4	51	72	complete
F35P17	2402	2555	Zirc-4	RT	FHT	zone1	52	117	Future test with aerosol collection

* FHT = full-length fuel rod heat treatment

E-2.1 Test Procedure and Data Processing

E-2.1.1 Test Protocol

Instrument and software testing equipment description:

Load frame	Instron 5967
Bend fixture capacity:	30 kN
Voltage:	110/220 V
Software:	Bluehill-3
Furnace:	CP122117 Environmental Chamber and Control Unit
Furnace max temperature:	≤400°C
Scale:	Ohaus Scout NV1201

The 4PB fixture was adjusted and the fixed positions measured before being inserted into the hot cell. The lower support positions are fixed at 5 in. center-to-center, and the upper loading positions are fixed at 1.67 in. center-to-center. The upper fixture is centered on the lower fixture, providing a symmetric loading of the rod specimen. Calibration of the Instron load cell and displacement and uncertainty evaluations for the four-point bend test are provided in Appendix H of this report.

Each test specimen is stored separately, and only one specimen is removed from its labeled storage container at a time. Each specimen is weighed and then placed on the lower 4PB support fixture and pushed back until it rests against the provided stops. The upper 4PB fixture is lowered to within ~1/32 in. of the top of the test specimen.

If the test will be at temperature, then the furnace door is closed, and heating is initiated. During heating, the upper 4PB fixture is raised as needed to avoid preload of the specimen caused by thermal expansion of the system.

Once the system is at the specified temperature, the upper 4PB fixture is lowered to contact with the test specimen, as indicated by an increase in load. Care is taken to keep the amount of initial loading small.

The test system is then zeroed, and the test is initiated. All tests are run using a fixed displacement speed of 0.050 mm/s. The load and crosshead displacement are collected for the entire test, and the test proceeds until the specimen is fractured.

Following fracture, the specimen, as defined by the fueled pieces within the cladding, is weighed. Any loose particles are weighed. The post-test specimen is placed in a labeled capsule and returned to storage.

E-2.1.2 Corrections for Machine Compliance

The load vs. crosshead extension data necessarily include information on machine compliance. When the load frame applies a force, the entire system, including the frame, load cell, grips, couplings, and specimen, experiences some amount of deflection. The load frame's reported displacement is the sum of the entire system's deformation. To determine the displacement of the specimen only, the machine compliance (deformation associated with the load frame, load cell, and grips) is removed from the load frame's reported displacement data.

Machine compliance is measured by testing a rigid specimen using the 4PB setup. In this case, a high-strength steel rod (OD = 2.00 in.) was used. The corrected displacement is calculated by subtracting the displacement reported in the machine compliance test from the displacement reported in the test of each sister rod specimen.

Because the 4PB specimen fractures at a load that is much lower than the load frame's limit (typically less than 10% of capacity), the corrections made to the 4PB displacements are small.

E-2.1.3 Test Specimen

Rough-cut 152 mm (6 in.) long fueled segments are used directly for 4PB. The specimens are unpressurized and have open ends.

E-2.1.4 Data Reduction

The 4PB test can be evaluated using simple beam theory given the nominal dimensions of the rod specimen and test fixture, idealizing the composite fuel rod segment as a solid cylindrical geometry made of an isotropic material. The uncertainties associated with these assumptions are discussed within this Appendix E and are further evaluated with respect to the measurement uncertainty in Appendix H of this report.

The four-point loaded beam is preferred for determining strength properties because the center span is uniaxially stressed (i.e., no shear stresses exist). The bending moment applied is constant over the inner span between the two upper fixture loading points. The load applied on the specimen at each fixture loading point, P, is half the load recorded by the load frame. The deflection of the specimen at the loading points, Δ_f, is the measured crosshead displacement of the upper test fixture recorded by the load frame minus the machine compliance.

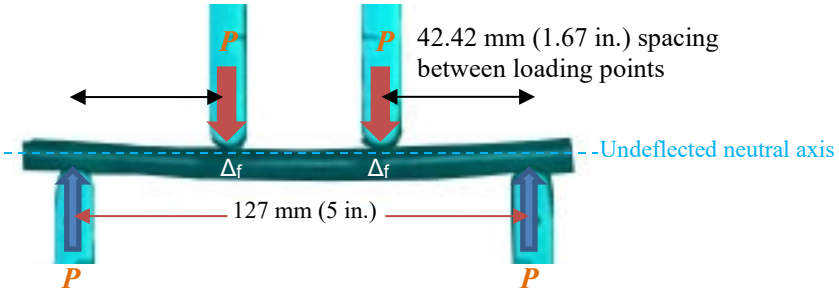

Figure E-4. Simple beam representation of the 4PB test.

The idealized composite rod performance is evaluated using classical elastic beam theory. As a reminder, many of the assumptions inherent in beam theory are not met within the composite rod, including the following:

- As previously discussed, an SNF composite rod is not a homogeneous isotropic material.
- Transverse planes perpendicular to the longitudinal axis of the composite rod might not remain planar after it is deflected because of the many cracks and discontinuities inherent in the pellet stack.
- It is unclear whether any local plastic strain or twist of the rod occurs during the test.

Nevertheless, beam theory is used to provide points of comparison of the SNF composite rod response under a bending load with other engineered materials.

To determine the maximum stress and strain on the specimen, the maximum bending moment between load upper loading points, M_{max}, is calculated using the spacing between the fixed support and the moving loading points and the load at each loading point (the load reported by the load frame divided by two):

$$42.42\ mm\ P. \tag{E-1}$$

Using classical beam theory, Δmax, the maximum beam deflection at the idealized rod's axial center, can be calculated as

$$\frac{Pa}{24EI}(3l^2 - 4a^2) = \frac{42.42\ mm\ P}{24EI}(3[127\ mm]^2 - 4[42.42\ mm]^2), \tag{E-2}$$

where *E* is the elastic modulus of the idealized fuel rod (assuming that it is a single material having a solid circular cross-section), and *I* is the first moment of inertia, approximated as $\frac{1}{4}\pi\left(\frac{OD}{2}\right)^4 \approx 400\ mm^4$; the product *EI* is referred to as the idealized rod's flexural rigidity. Simplifying,

$$\Delta\,\text{max} = \frac{182.1\ mm^{-1} * P\ (in\ N)}{E\ (in\ N/mm^2)}. \tag{E-3}$$

Δ_f can also be related to the elastic modulus of the composite fuel rod using beam theory:

$$\frac{Px}{6EI}(3la - 3a^2 - x^2) = \frac{42.42P}{6EI}(3 * 127\ mm * 42.42\ mm - 3[42.42\ mm]^2 - [42.42\ mm]^2),$$

which simplifies as:

$$\frac{158.5\ mm^{-1} * P\ (in\ N)}{E\ (in\ N/mm^2)}, \tag{E-4}$$

and allowing an estimate of the idealized single-material, solid circular section elastic modulus:

$$E = \frac{158.5\ mm^{-1} * P\ (in\ N)}{\Delta_f}. \tag{E-5}$$

Substituting Eq. (E-5) into Eq. (E-3) yields an estimate of the maximum deflection at the center of the 4PB specimen for use in calculating the maximum stress and strain:

$$\Delta\text{max} = (182.1 / 158.5)\ \Delta_f. \tag{E-6}$$

The maximum stress, σ_{max}, of the idealized composite rod segment is estimated as

$$\frac{42.42\ mm\ P\ (OD/2)}{I}. \quad \text{(E-7)}$$

For more accurate estimates, the measured outer diameter (OD) of the rod at the segment elevation [E-7] is used.

The radius of curvature, ρ, is calculated using the displacements Δ_f and Δ_{max} assuming the displaced shape of the fuel rod segment in the region of pure bending is circular, as described in Appendix F, and the maximum strain on the idealized rod segment, ε, is calculated as

$$\frac{(OD/2)}{\rho}. \quad \text{(E-8)}$$

Ideally, the elastic modulus is equivalent to the flexural, or *bending*, modulus. Realistically, these values might be different. An elastic modulus, *E*, is evaluated from the test data as the slope of a least-squares fit line to the stress-strain data in the elastic region, and a plastic modulus, E_p, is evaluated as the slope of a least-squares fit line to the stress-strain data in the plastic region above the evaluated yield point. The elastic and plastic average flexural rigidities are calculated by multiplying *E* and E_p by the tested segment's calculated *I*.

To summarize, idealization of the fuel rod segment as a simplified elastic beam is used here as a practical approach to evaluate the test data and allow for comparisons with other materials, but the resulting evaluated properties should not be considered cladding material properties. Also, *elastic* beam equations are used to evaluate yield strength and ultimate strength for the idealized fuel rod segment. Elastic theory isn't strictly applicable in the plastic region (here defined as the region of the load versus displacement and stress versus strain that departs from linearity), but the strain at fracture is relatively small and deviation from elastic theory is therefore expected to be small. To verify this assumption, measurements were taken in the plastic region using the visual record of the tests. It should be noted that the video record was not planned to be used for this purpose, and not all of the video records were usable for this purpose. The measured ratio Δ_{max}/Δ_f ranged from 1.129 to 1.161 (average of 1.148 for the 7 tests measured) just beyond the yield point, and from 1.127 to 1.159 (average of 1.144 for the 8 tests measured) very near the point where fracture occurred. Elastic theory predicts the ratio as 1.149 for the test setup used.

E-2.2 Measured Load and Displacement Data

The load vs. crosshead extension (i.e., displacement of the fixture) was recorded for each test and is provided in Figure E-5 for the baseline and heat-treated Zirc-4-clad and LT Zirc-4-clad specimens, in Figure E-6 for the baseline and heat-treated M5-clad specimens, and in Figure E-7 for the baseline and heat-treated ZIRLO-clad specimens. Figure E-8 plots the RT tests, and Figure E-9 plots the 200°C tests.

E-2.3 Calculated Stress, Strain, 0.2% Offset Yield, Flexural Strength, and Flexural Rigidity

Using the simplified elastic beam approach discussed in Section E-2.1.4, stress and strain were calculated and are graphed in Figure E-10 at RT and Figure E-11 at 200°C. The flexural modulus, modulus of rigidity (EI), 0.2% offset yield strength, and flexural strength were also calculated. The supporting

measured and calculated data are summarized in Table E-2, and they are plotted with specimen average burnup in Figure E-12 for RT tests and in Figure E-13 for 200°C tests. The uncertainty associated with these results was evaluated in Appendix H. The elastic flexural rigidity measured using 4PB is in good agreement with the dynamic rigidity measurements using the cyclic integrated reversible-bending fatigue tester (CIRFT) (see Appendix F), as shown in Figure E-14.

The heat-treated M5 and ZIRLO-clad specimens generally have higher ductility than the baseline specimens, but it is difficult to come to any firm conclusions with the limited data available.

Table E-2. Measured and calculated 4PB data.

Test specimen	Cladding alloy	Heat-treatment	Estimated burnup (GWd/MTU) [E-7]	Test temp. (°C)	Average specimen OD [E-7]	Crosshead extension, Δ_f, at failure (mm)	Maximum deflection, Δmax, at failure (mm)*	0.2% yield strength (MPa)*	Flexural strength (MPa)
30AD05-1299-1452	M5	---	60	25.7	9.423	8.33	9.57 ± 0.09	533 ± 11	641 ± 13
30AE14-0978-1131	M5	FHT	59	26.6	9.459	11.69	13.43 ± 0.13	481 ± 10	609 ± 12
3D8E14-1025-1178	ZIRLO	---	64	25.3	9.500	7.41	8.51 ± 0.08	617 ± 12	766 ± 15
3F9N05-2063-2216	ZIRLO	FHT	59	24.7	9.471	10.64	12.22 ± 0.12	526 ± 10	717 ± 14
3A1F05-1279-1432	LT Zirc-4	---	57	26.4	9.465	7.47	8.59 ± 0.08	616 ± 12	768 ± 15
F35P17-1319-1472	Zirc-4	FHT	52	24.9	9.503	5.36	6.16 ± 0.06	555 ± 11	640 ± 13
F35P17-1472-1625	Zirc-4	FHT	53	27.2	9.531	6.52	7.49 ± 0.07	565 ± 11	693 ± 14
30AD05-0850-1003	M5	---	60	200.0	9.429	5.77	6.63 ± 0.06	405 ± 8	461 ± 9
30AD05-1800-1953	M5	---	59	200.0	9.423	6.07	6.97 ± 0.07	443 ± 9	502 ± 10
30AE14-0825-0978	M5	FHT	58	200.0	9.457	11.60	13.33 ± 0.13	401 ± 8	503 ± 10
30AE14-2050-2203	M5	FHT	60	200.0	9.454	12.11	13.91 ± 0.13	385 ± 8	502 ± 10
3D8E14-0872-1025	ZIRLO	---	64	200.0	9.497	6.91	7.93 ± 0.08	518 ± 10	644 ± 13
3D8E14-1907-2060	ZIRLO	---	64	200.0	9.492	6.97	8.01 ± 0.08	460 ± 9	583 ± 12
3F9N05-0872-1025	ZIRLO	FHT	59	200.0	9.465	7.89	9.07 ± 0.09	461 ± 9	583 ± 12
3F9N05-1910-2063	ZIRLO	FHT	59	200.0	9.469	9.15	10.51 ± 0.10	448 ± 9	588 ± 12
3A1F05-1432-1585	LT Zirc-4	---	56	200.0	9.459	5.03	5.78 ± 0.06	519 ± 10	589 ± 12
3A1F05-2230-2383	LT Zirc-4	---	54	200.0	9.480	4.91	5.64 ± 0.05	481 ± 10	550 ± 11
F35P17-2230-2383	Zirc-4	FHT	51	200.0	9.514	7.50	8.61 ± 0.08	461 ± 9	588 ± 12
				Average at RT:		8.20	9.42 ± 0.09	556 ± 11	691 ± 14
				Average at 200°C:		7.63	8.76 ± 0.08	453 ± 9	554 ± 11

Table E-2. Measured and calculated 4PB data (continued).

Test specimen	Cladding alloy	Heat-treatment	Estimated burnup (GWd/MTU) [E-7]	Test temp. (°C)	Average specimen OD [E-7]	Failure strain (%)*	Flexural modulus (GPa)	Elastic region flexural rigidity (N-m^2)	Plastic region flexural rigidity (N-m^2)*
30AD05-1299-1452	M5	---	60	25.7	9.423	2.6 ± 0.04	57.88 ± 1.45	22.4 ± 0.5	1.9 ± 0.04
30AE14-0978-1131	M5	FHT	59	26.6	9.459	3.8 ± 0.06	57.17 ± 1.43	22.5 ± 0.5	1.1 ± 0.03
3D8E14-1025-1178	ZIRLO	---	64	25.3	9.500	2.3 ± 0.04	58.04 ± 1.45	23.2 ± 0.5	5.1 ± 0.12
3F9N05-2063-2216	ZIRLO	FHT	59	24.7	9.471	3.3 ± 0.06	55.34 ± 1.38	21.9 ± 0.5	3.9 ± 0.09
3A1F05-1279-1432	LT Zirc-4	---	57	26.4	9.465	2.3 ± 0.04	59.25 ± 1.48	23.3 ± 0.5	6.7 ± 0.15
F35P17-1319-1472	Zirc-4	FHT	52	24.9	9.503	1.7 ± 0.03	54.24 ± 1.36	21.7 ± 0.5	8.5 ± 0.20
F35P17-1472-1625	Zirc-4	FHT	53	27.2	9.531	2.2 ± 0.04	54.72 ± 1.37	22.2 ± 0.5	6.2 ± 0.14
30AD05-0850-1003	M5	---	60	200.0	9.429	2.0 ± 0.03	51.44 ± 1.29	20.0 ± 0.5	2.0 ± 0.04
30AD05-1800-1953	M5	---	59	200.0	9.423	2.0 ± 0.03	53.60 ± 1.34	20.7 ± 0.5	2.2 ± 0.05
30AE14-0825-0978	M5	FHT	58	200.0	9.457	3.7 ± 0.06	55.97 ± 1.40	22.0 ± 0.5	0.8 ± 0.02
30AE14-2050-2203	M5	FHT	60	200.0	9.454	4.6 ± 0.08	53.66 ± 1.34	21.0 ± 0.5	1.2 ± 0.03
3D8E14-0872-1025	ZIRLO	---	64	200.0	9.497	2.2 ± 0.04	54.09 ± 1.35	21.6 ± 0.5	4.7 ± 0.11
3D8E14-1907-2060	ZIRLO	---	64	200.0	9.492	2.2 ± 0.04	50.97 ± 1.27	20.3 ± 0.5	4.7 ± 0.11
3F9N05-0872-1025	ZIRLO	FHT	59	200.0	9.465	2.5 ± 0.04	50.60 ± 1.27	19.9 ± 0.5	3.5 ± 0.08
3F9N05-1910-2063	ZIRLO	FHT	59	200.0	9.469	2.9 ± 0.05	50.64 ± 1.27	20.0 ± 0.5	3.3 ± 0.08
3A1F05-1432-1585	LT Zirc-4	---	56	200.0	9.459	1.6 ± 0.03	54.27 ± 1.36	21.3 ± 0.5	7.4 ± 0.17
3A1F05-2230-2383	LT Zirc-4	---	54	200.0	9.480	1.6 ± 0.03	51.25 ± 1.28	20.3 ± 0.5	6.9 ± 0.16
F35P17-2230-2383	Zirc-4	FHT	51	200.0	9.514	2.4 ± 0.04	48.77 ± 1.22	19.6 ± 0.5	4.3 ± 0.10
				Average at RT:		2.6 ± 0.04	56.66 ± 1.42	22.5 ± 0.6	5.7 ± 0.11
				Average at 200°C:		2.4 ± 0.04	52.30 ± 1.31	20.6 ± 0.5	4.4 ± 0.09

* These values are based on the calculated maximum specimen deflection using elastic beam theory as described in Section E-2.1.4.

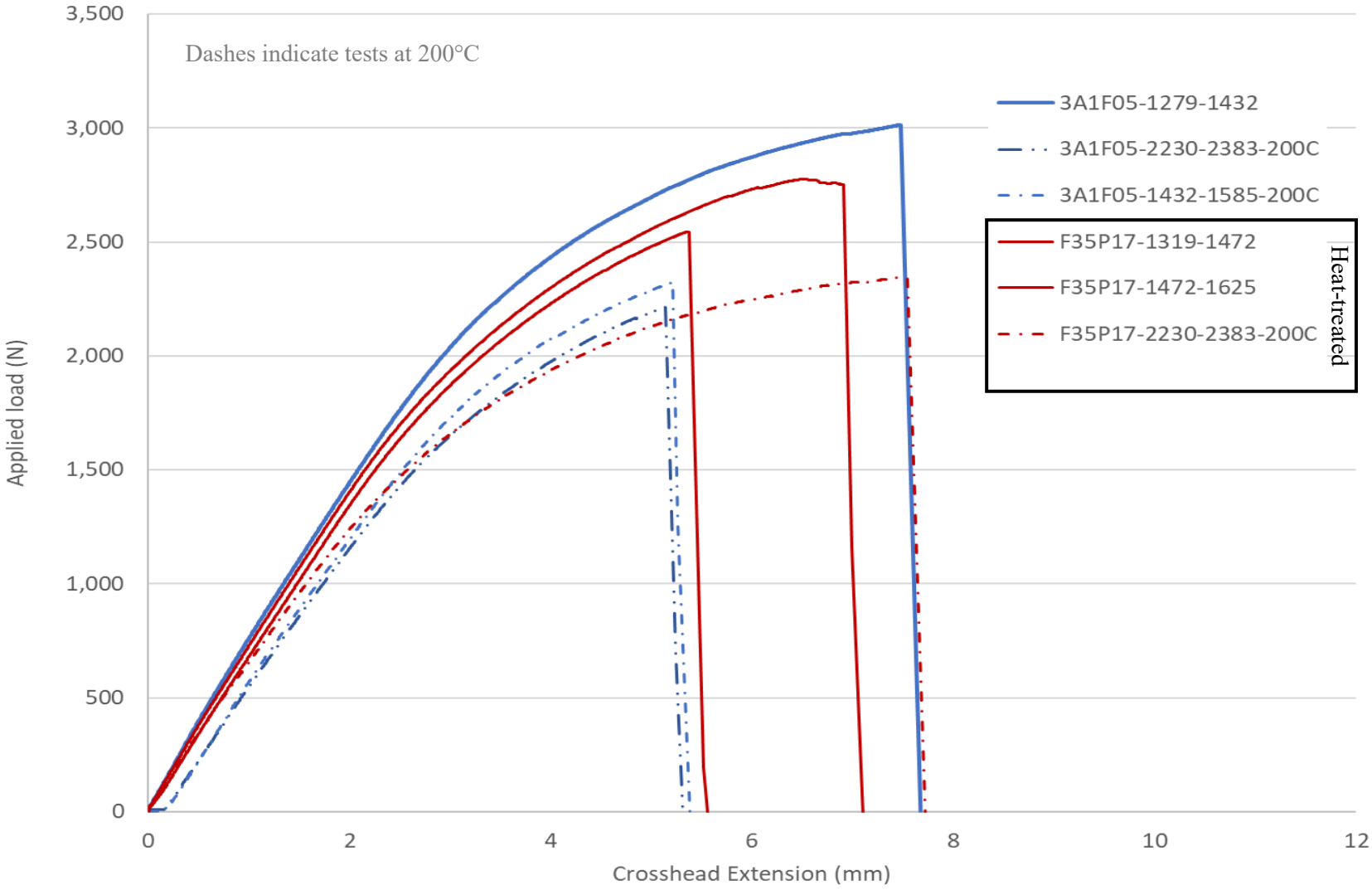

Figure E-5. Zirc-4 and LT Zirc-4 specimens, load vs. crosshead extension.

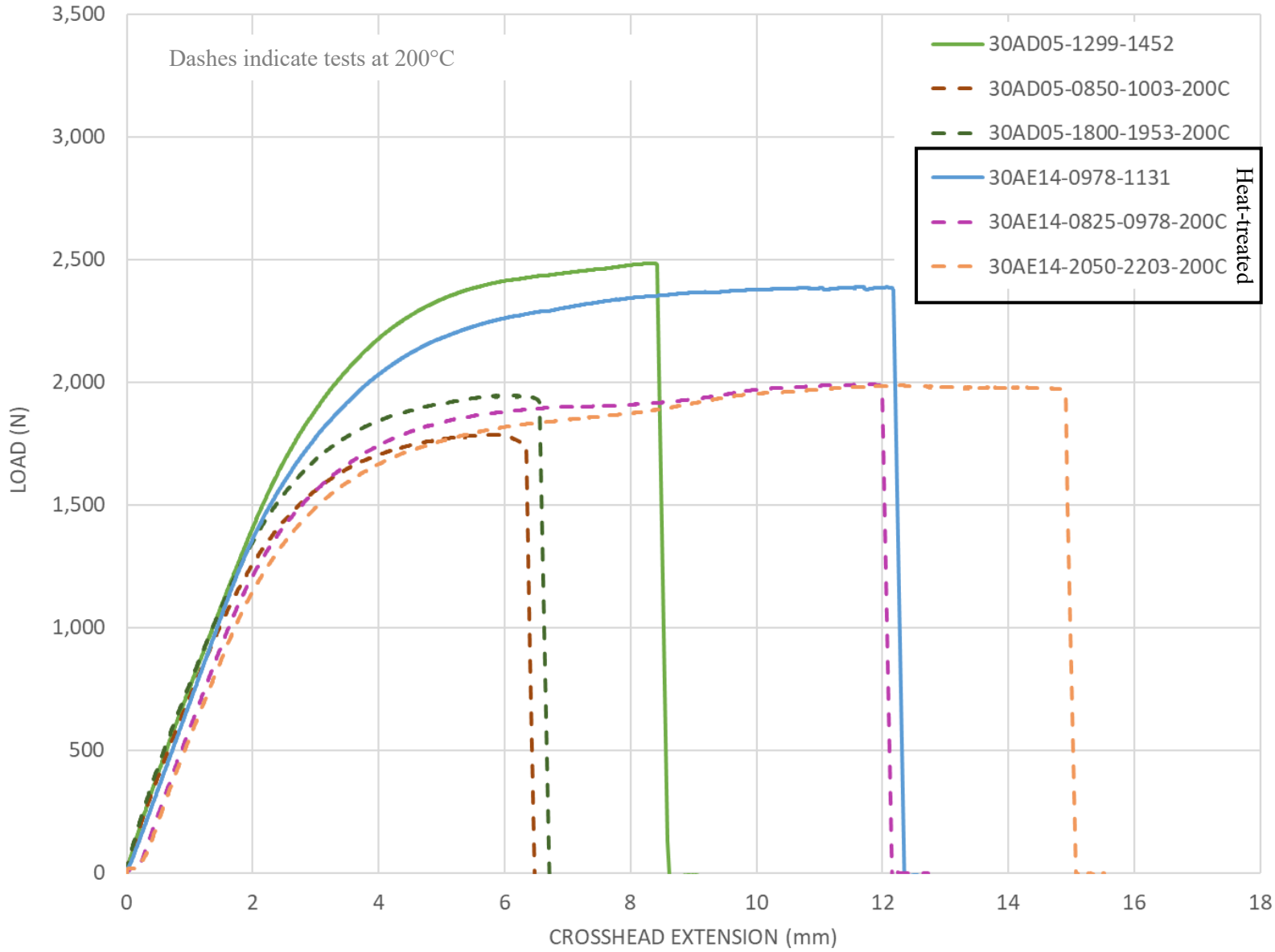

Figure E-6. M5 specimens, load vs. crosshead extension.

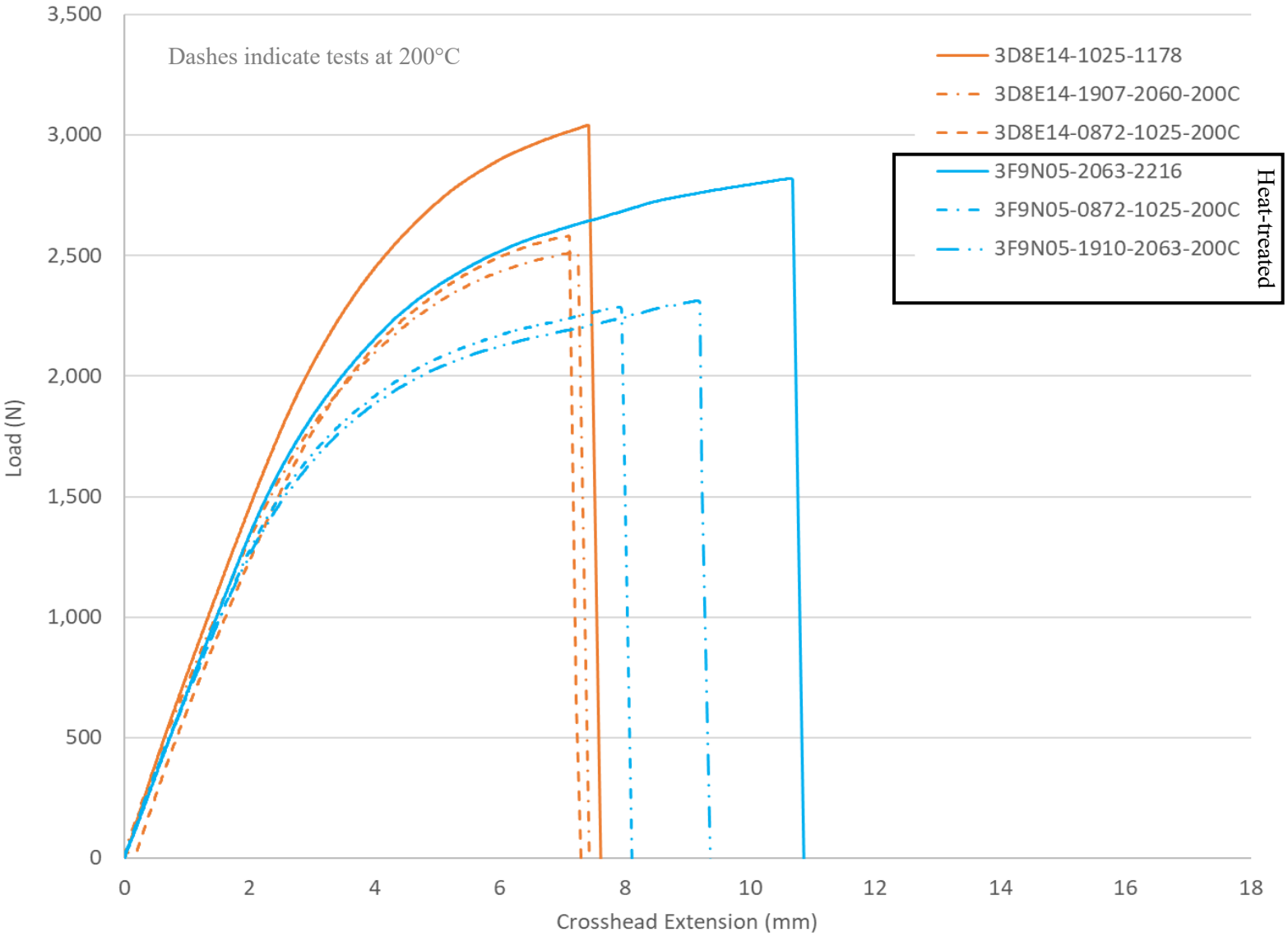

Figure E-7. ZIRLO specimens, load vs. crosshead extension.

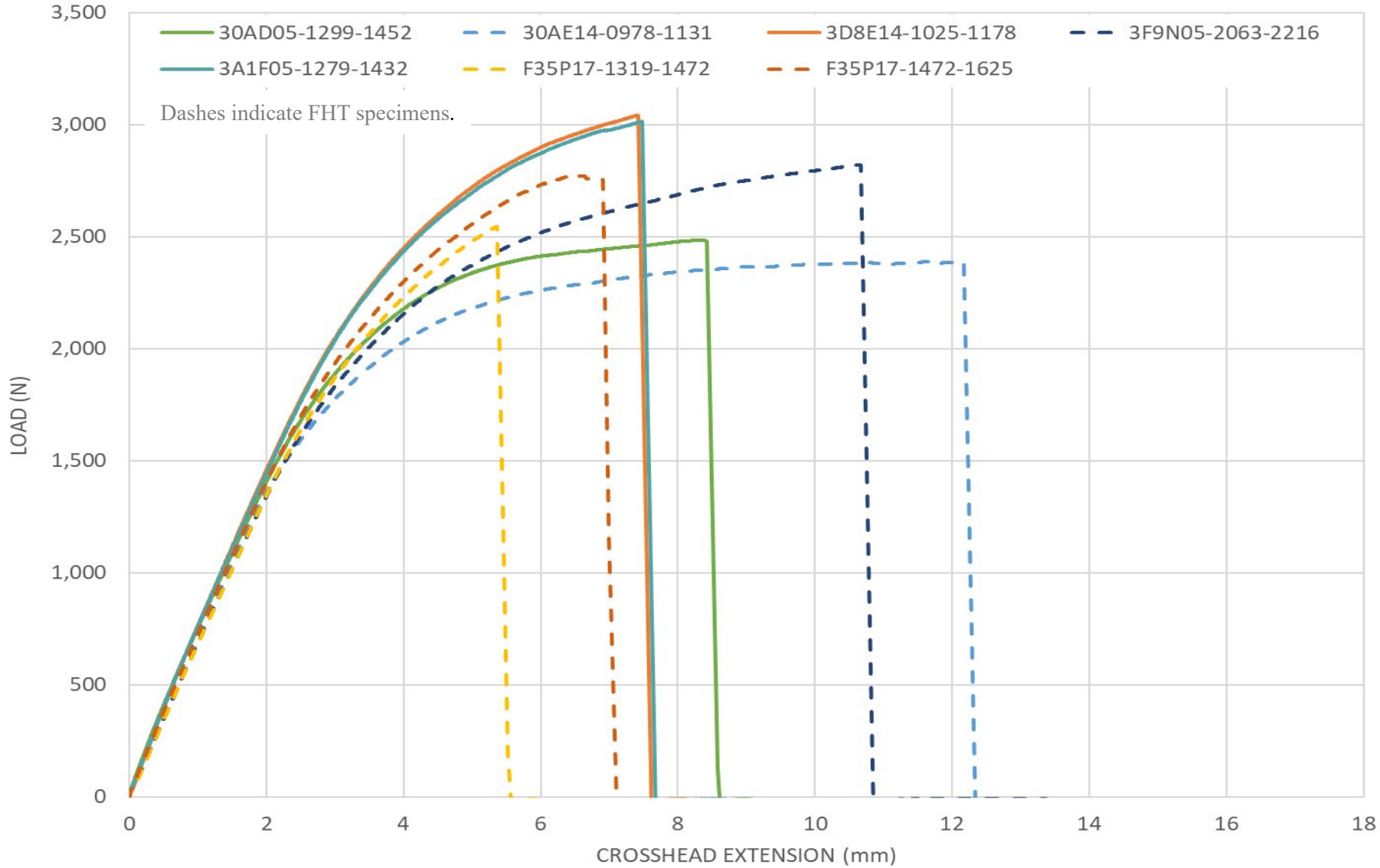

Figure E-8. Load vs. crosshead extension for all RT tests.

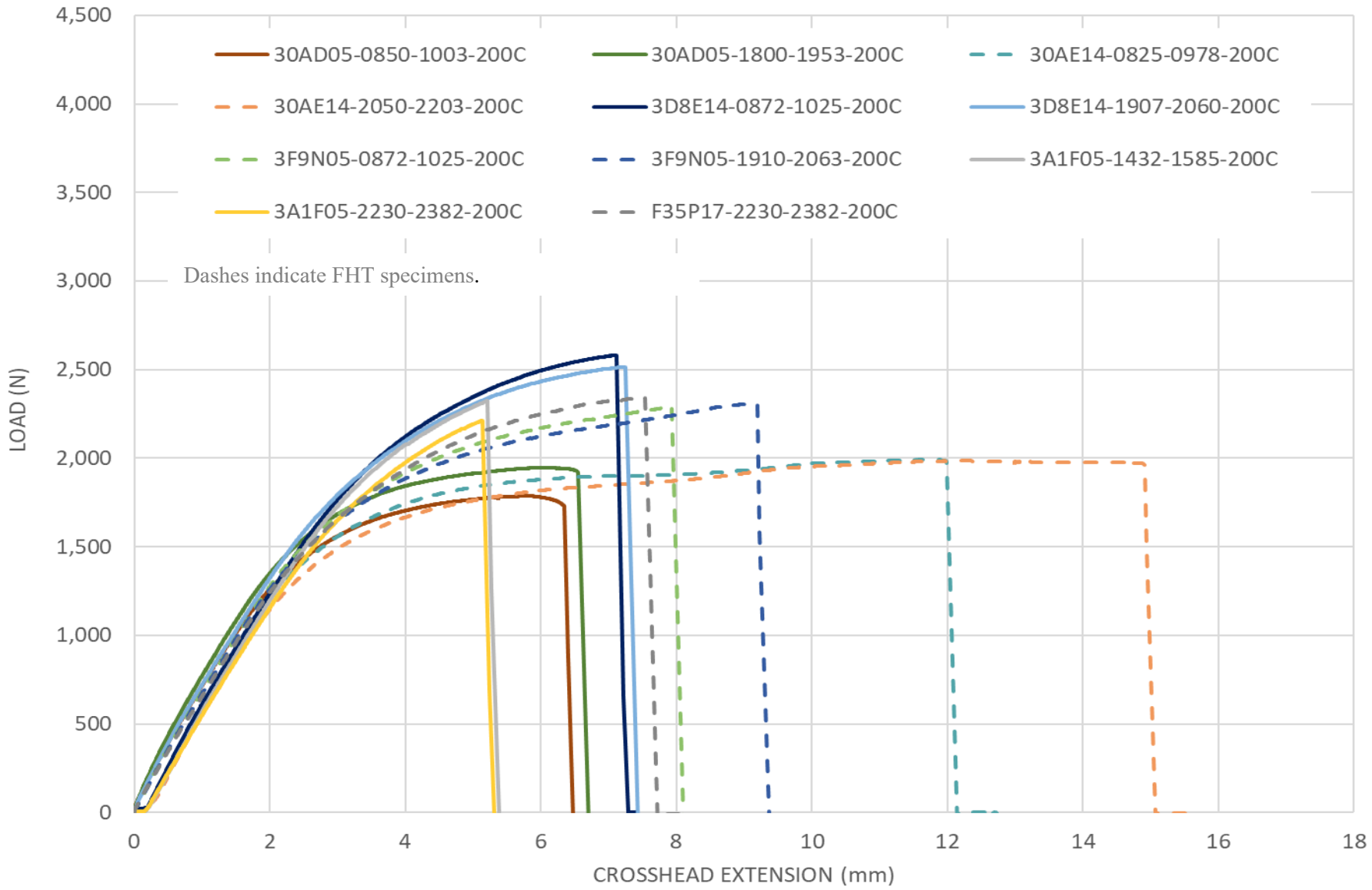

Figure E-9. Load vs. crosshead extension for all 200°C tests.

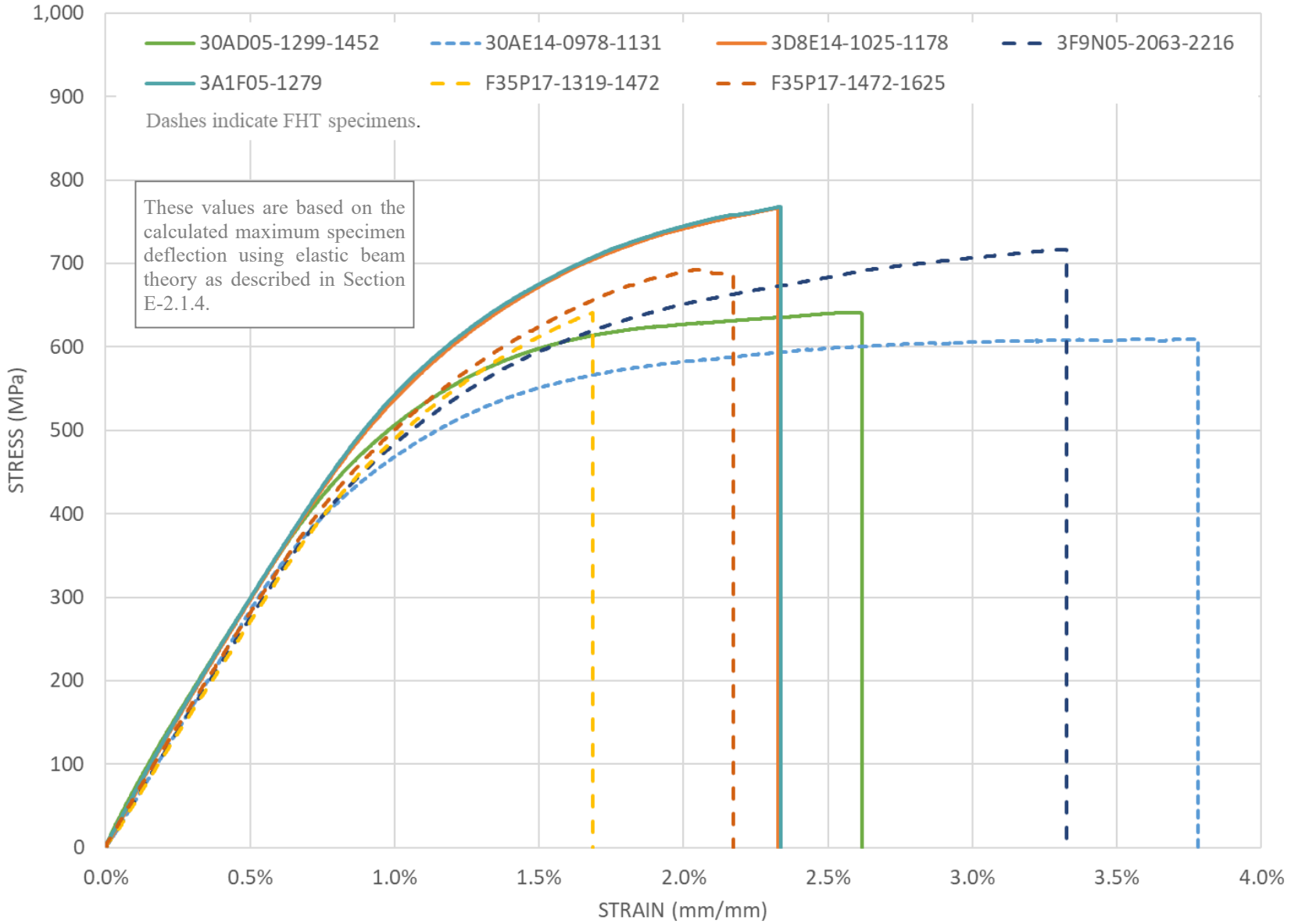

Figure E-10. Stress vs. strain plot for RT data.

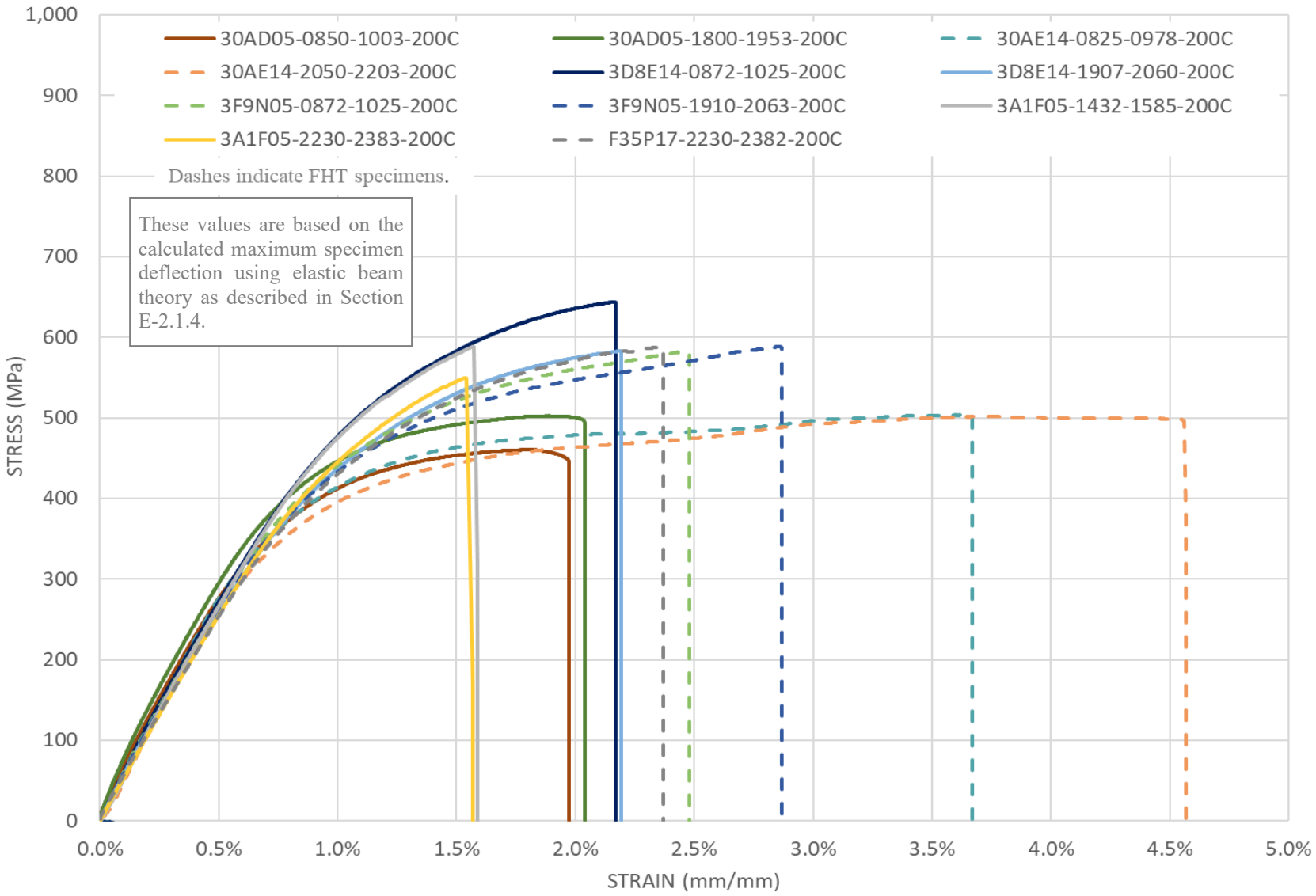

Figure E-11. Stress vs. strain plot for 200°C data.

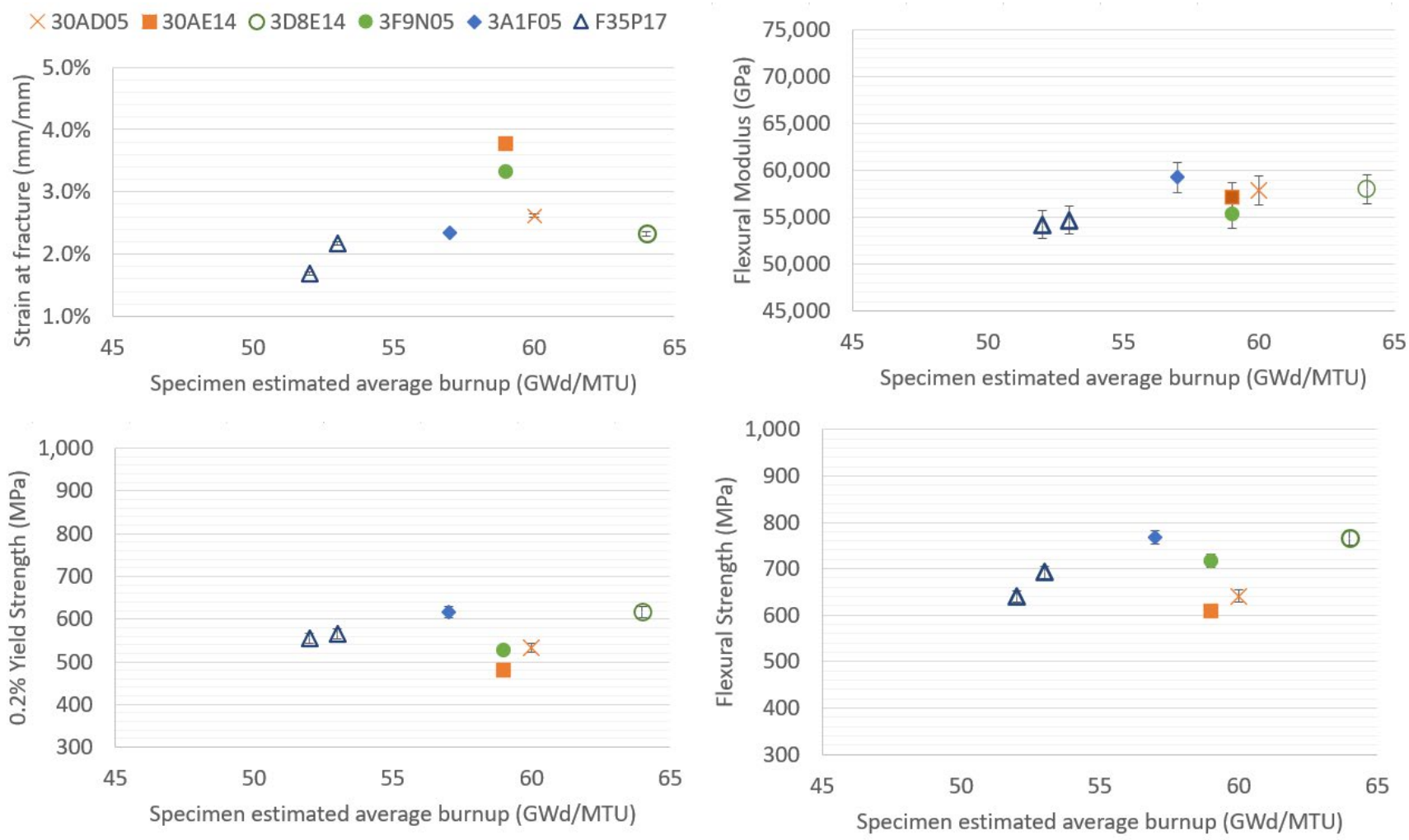

Figure E-12. Calculated RT data plotted as a function of specimen average burnup.

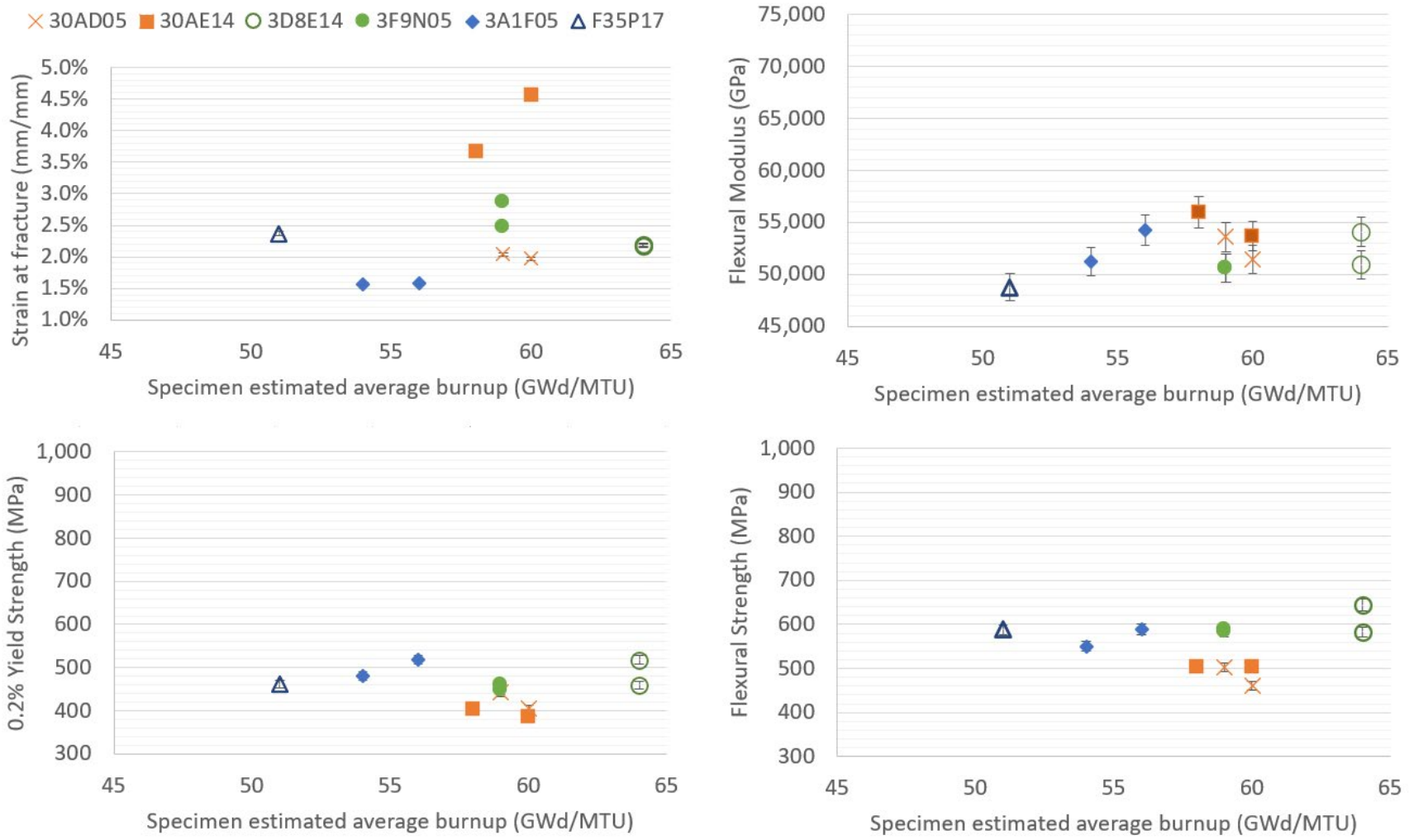

Figure E-13. Calculated 200°C data plotted as a function of specimen average burnup.

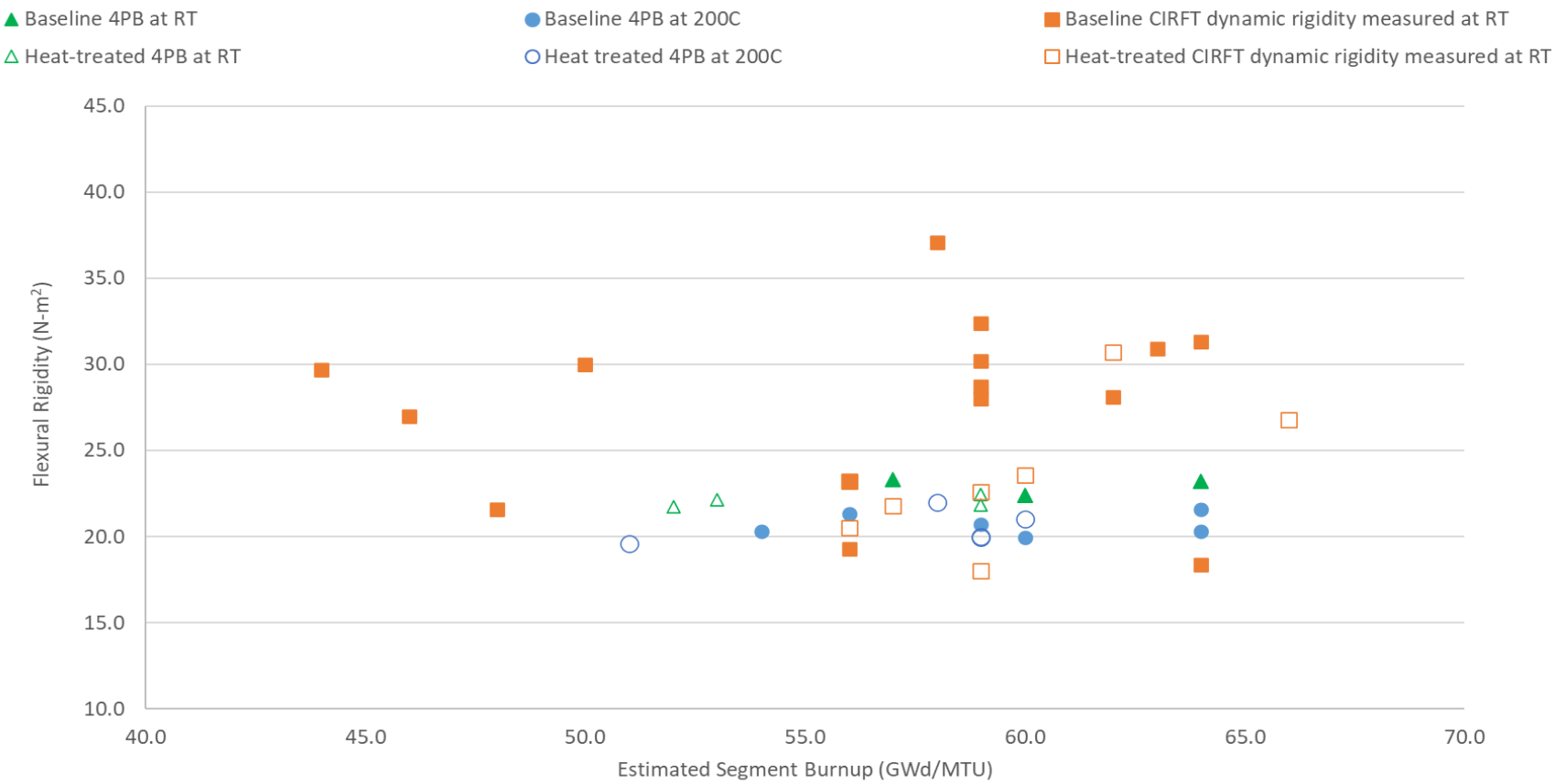

Figure E-14. Comparison of the CIRFT-measured elastic dynamically measured flexural rigidity (as discussed in Appendix F) and the 4PB-measured elastic rigidity.

E-2.4 Typical Fracture Observed

All segments were fractured near the center of the segment and in the gauge section. Many segments did not fracture completely through the rod section, as shown in Figure E-15(a). Although detailed imaging has not yet been completed, many segments appeared to fracture at pellet-pellet interfaces, as shown in Figure E-15(b). Other specimens fractured through the complete section with tearing of the cladding, as shown in Figure E-16(a) and Figure E-16(b), and the fracture also occurred in the body of the pellet.

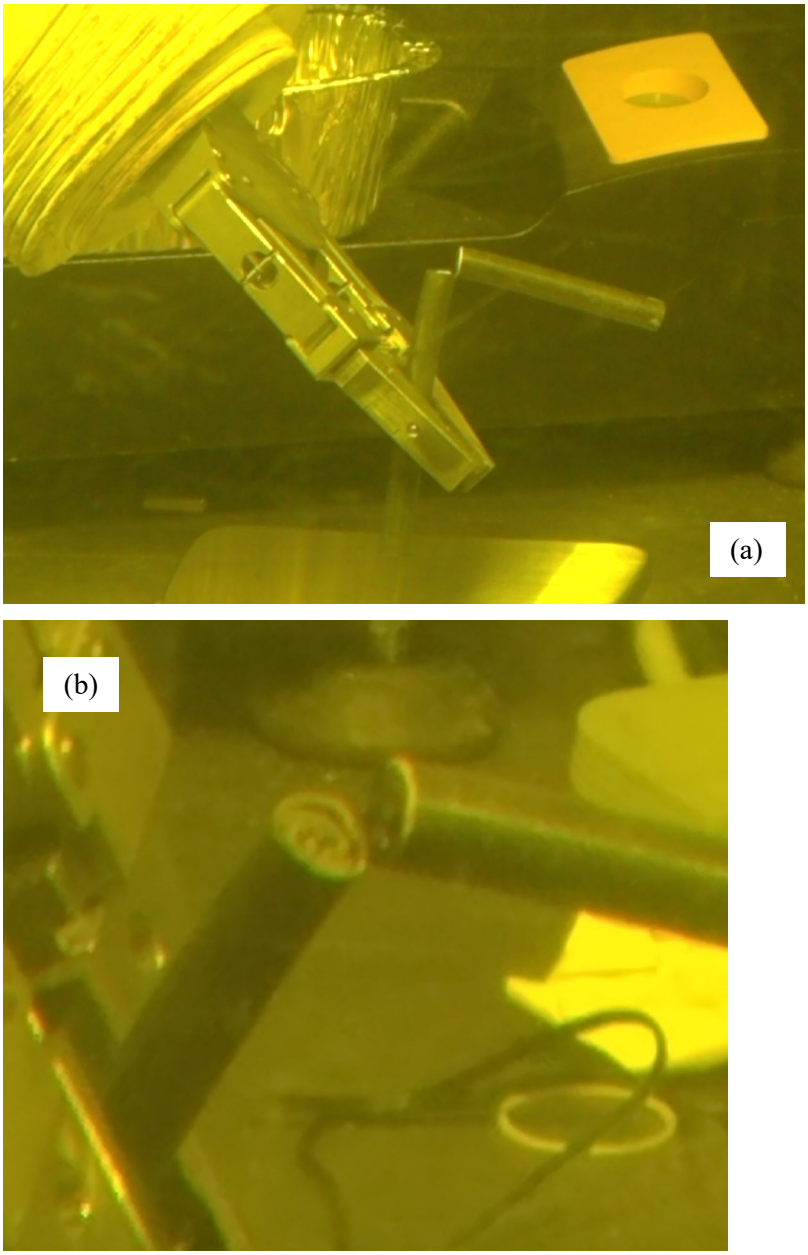

Figure E-15. (a) Many specimens did not completely fracture and (b) fractured at pellet-pellet interfaces.

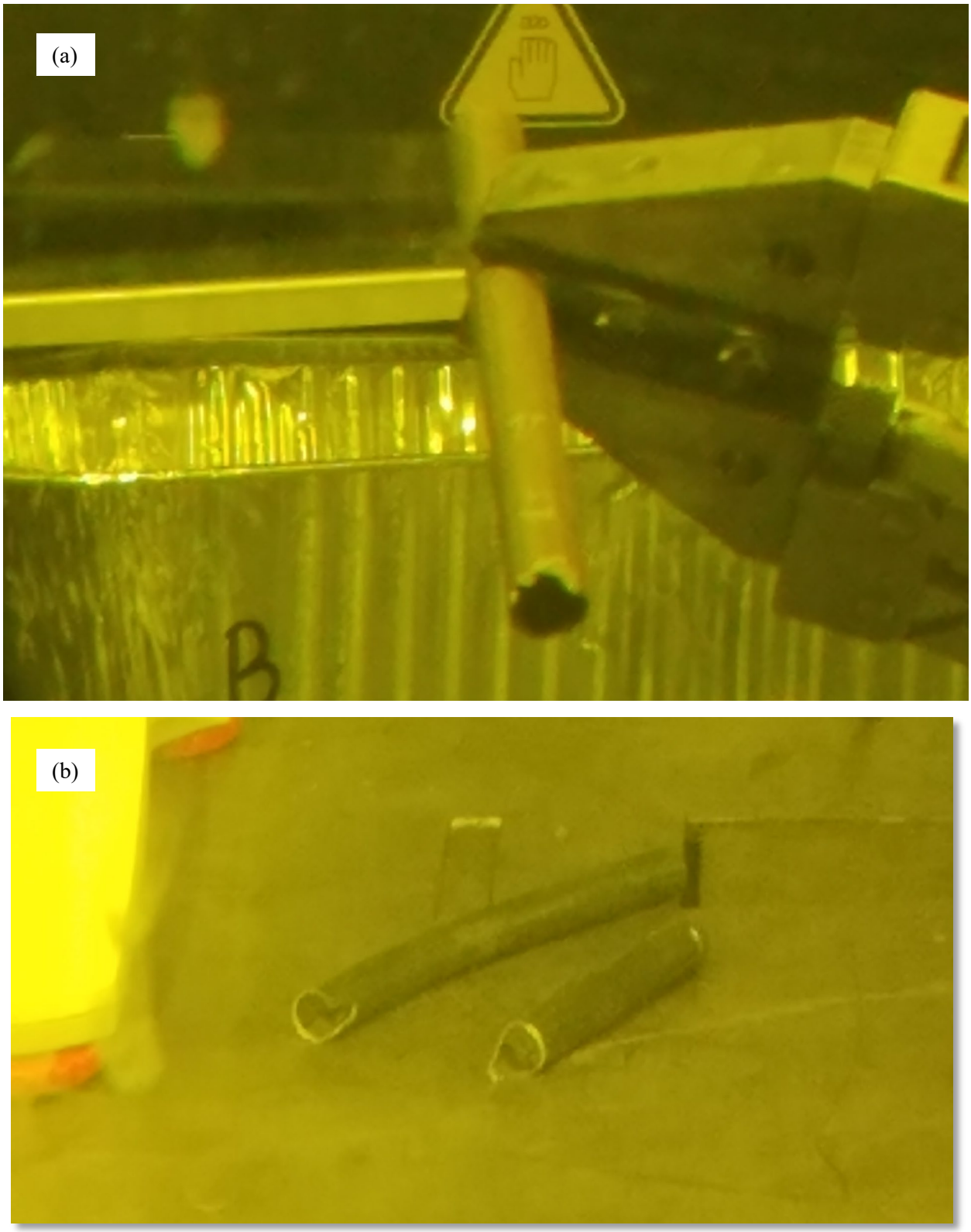

Figure E-16. (a) An example of through-section fracture with secondary tearing, and (b) fracture that occurred in the body of the pellet.

E-2.5 Fuel Release During Fracture

The amount of fuel released during fracture was determined by weighing each specimen before and after the test and weighing the debris collected. Figure E-17 provides a histogram of the mass loss for all specimens tested in 4PB. The largest difference from pre-test to post-test weight was 1.7 ± 0.1 g for F35P17-1472-1625 (RT test). Based on Figure E-18, there is no trend of mass loss with test temperature or burnup. There is a tendency for the RT tests to have more mass loss, likely because the cladding fracture is more energetic than the 200°C fracture. From the nondestructive examination (NDE) [E-7] results, each pellet is 9.9–13.7 mm long on average[a] for the sister rods, and each pellet weighs approximately 5.1–7.0 g, assuming a density of 10.1 g/cc. Therefore, the maximum mass lost represents about ¼ of a pellet, whereas the more typical 0.4 g mass loss is less than ⅒ of a full pellet.

The catch tray placed below each specimen during testing collected most of the debris. As shown in Figure E-19(a) and (b), when fracture occurred at pellet-pellet ends, the debris consisted of small particles. A more rigorous method of capturing and quantifying dust-type debris has been implemented and is described in Appendix I.

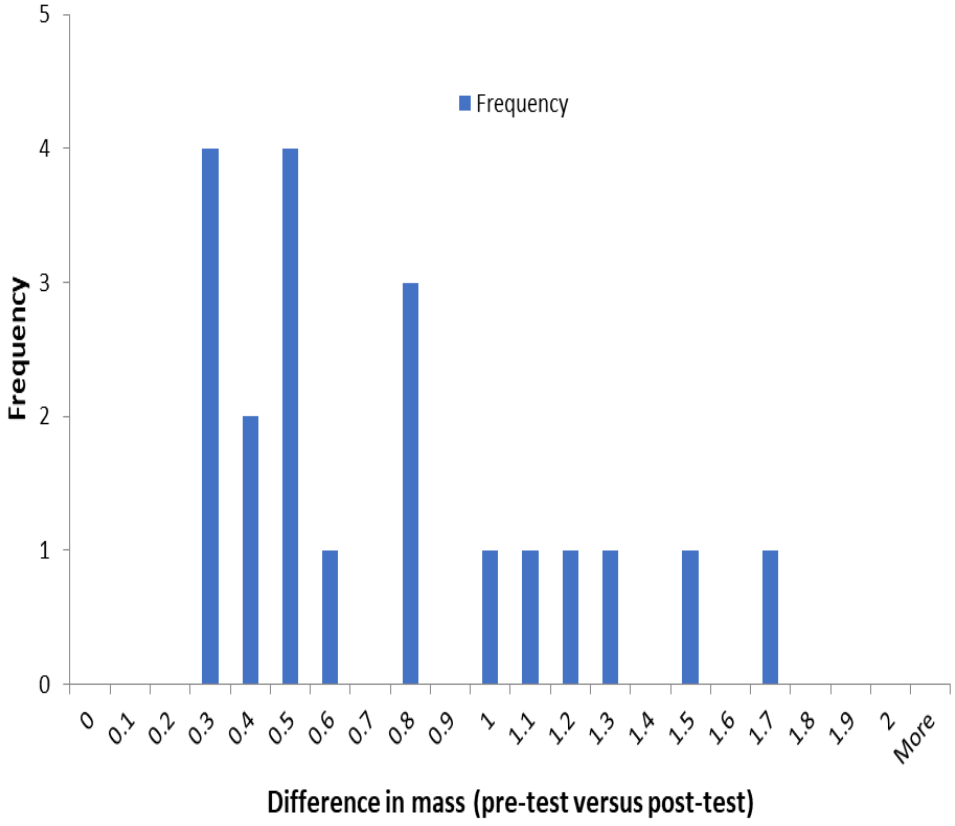

Figure E-17. Histogram of mass loss resulting from 4PB test.

[a]ZIRLO-, M5-, and LT Zirc-4-clad rods have measured pellet lengths from 9.8 to 10.3 mm, and the Zirc-4 clad rods have measured pellet length from 13.6 to 13.7 mm.

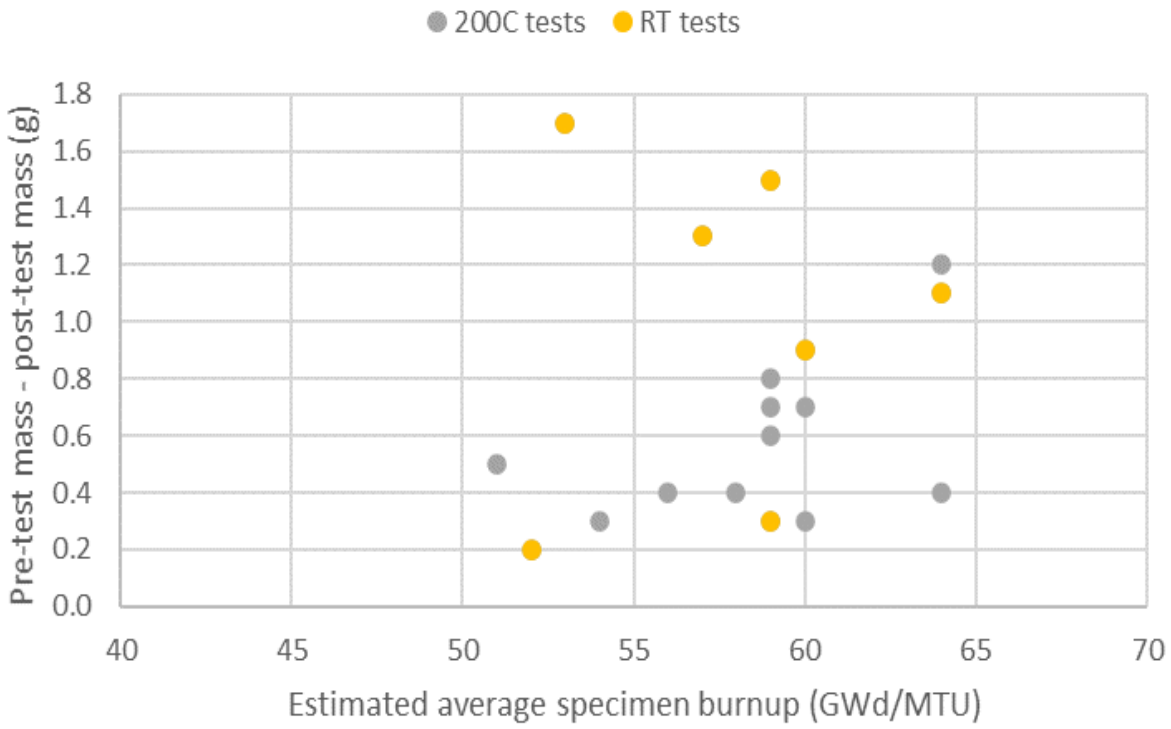

Figure E-18. Measured specimen mass differential (pre-test and post-test) as a function of estimated average specimen burnup.

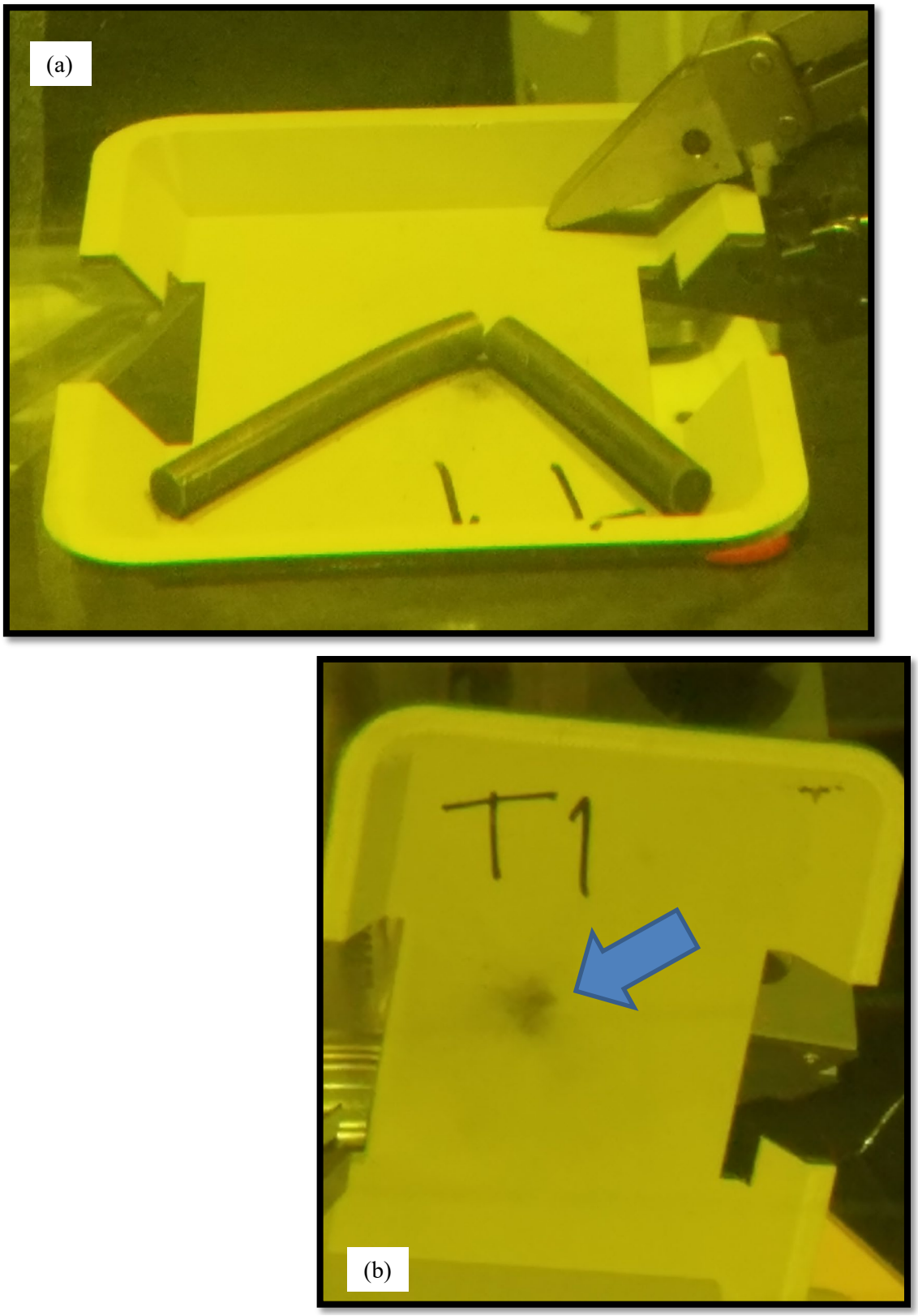

Figure E-19. (a) Post-test debris was captured by a catch tray located below the specimen with (b) the typical RT debris field composed of small particles.

E-3. Axial Tension Testing

To perform axial tension testing (DE.08), a small amount of fuel must be dissolved from each end of the specimen so that a grip can be inserted. The grip is used to prevent the specimen from being crushed at the load point. Therefore, although the rough-cut segments are available, they must be further processed to prepare them for the test. Table E-3 lists the specimens to be tested.

Table E-3. List of specimens for axial tension testing.

Specimen ID#			Test temperature	Specimen heat treatment before test	Operation zone	Specimen average burnup	Specimen average oxide thickness (μ)	Specimen alloy
30AE14	1574	1677	RT	FHT	zone1	59708	6	M5
30AD05	1452	1555	RT	None	zone1	59689	4	M5
30AE14	2300	2403	RT	FHT	zone1	59703	12	M5
30AD05	2802	2905	RT	None	zone1	56939	10	M5
F35P17	808	911	RT	FHT	zone1	53356	17	Zirc-4
3A1F05	1604	1707	RT	None	zone1	56669	42	LT Zirc-4
F35P17	2754	2857	RT	FHT	grid5	48531	133	Zirc-4
3A1F05	2754	2857	RT	None	grid5	52550	133	LT Zirc-4
3F9N05	1444	1547	RT	FHT	zone1	59480	12	ZIRLO
3D8E14	1553	1656	RT	None	zone1	64397	18	ZIRLO
3D8E14	2674	2777	RT	None	zone1	62923	44	ZIRLO
3F9N05	3138	3241	RT	FHT	zone1	55642	48	ZIRLO
30AE14	1471	1574	200°C	FHT	zone1	59199	5	M5
30AD05	1555	1658	200°C	None	zone1	59441	6	M5
30AE14	2403	2506	200°C	FHT	zone1	60227	13	M5
30AD05	3349	3452	200°C	None	zone1	49083	17	M5
F35P17	930	1033	200°C	FHT	zone1	53308	20	Zirc-4
3A1F05	1750	1853	200°C	None	zone1	56018	42	LT Zirc-4
F35P17	2857	2960	200°C	FHT	zone1	50566	138	Zirc-4
3A1F05	2857	2960	200°C	None	zone1	53978	138	LT Zirc-4
3D8E14	1450	1553	200°C	None	zone1	64219	16	ZIRLO
3F9N05	1547	1650	200°C	FHT	zone1	59371	13	ZIRLO
3D8E14	1804	1907	200°C	None	zone1	63962	19	ZIRLO
3F9N05	3035	3138	200°C	FHT	zone1	56996	48	ZIRLO

In FY21, Pacific Northwest National Laboratory (PNNL) reported a sensitivity of the cladding-only axial tension specimens associated with clamping the specimen into the load frame, as well as the clamp-on extensometer. PNNL also reported slipping of the specimen within the axial tension grips related to the specimen's OD oxide layer. ORNL has essentially an identical setup for axial tension tests. To determine if the sensitivity was also associated with fueled specimens, ORNL tested a specimen available from a previous program (M5 clad PWR rod). Four trials were performed, and the specimen broke each time at the clamp on the upper axial tension jaws. Based on these results, an alternative method to clamp the specimens in the load frame is being investigated.

E-4. Microhardness Tests

Microhardness test (DE.09) equipment is available at both the Low Activation Materials Development and Analysis (LAMDA) laboratory and the Irradiated Fuels Examination Laboratory (IFEL) at ORNL. The equipment at IFEL will be used for both RT and 200°C testing when it is available. The equipment at LAMDA has been used to perform tests at RT only. Table E-4 lists the specimens to be tested.

Table E-4. Specimens Selected for Microhardness Tests.

Rod	Originating segment elevation range (mm)		Cladding type	Estimated local burnup, GWd/MTU	Selection criteria
30AD05	3240	3259	M5	55	Highest oxide
30AD05	2410	2429	M5	59	HBU region with higher oxide
30AD05	1280	1299	M5	59	Oxide thickness and hydride distribution
30AE14	2675	2694	M5, heat-treated	61	HBU at oxide peak
30AE14	3399	3418	M5, heat-treated	50	Highest oxide thickness
3A1F05	2735	2754	LT Zirc-4	54	High oxide thickness at HBU
3A1F05	3105	3124	LT Zirc-4	53	Peak oxide thickness
3A1F05	2383	2402	LT Zirc-4	55	HBU with higher oxide thickness, spalling oxide, pellet banding
3A1F05	1260	1279	LT Zirc-4	56	Oxide thickness and hydride distribution
3A1F05	2006	2025	LT Zirc-4	56	Oxide thickness and hydride distribution
3D8E14	2655	2674	ZIRLO	63	HBU with oxide spike
3D8E14	3206	3225	ZIRLO	59	Highest oxide thickness
3D8E14	2303	2322	ZIRLO	62	Oxide thickness and hydride distribution
3D8E14	700	719	ZIRLO	62	Oxide thickness and hydride distribution
3F9N05	2863	2882	ZIRLO, heat-treated	58	HBU with higher oxide
3F9N05	3331	3350	ZIRLO, heat-treated	51	Peak oxide thickness, spalling oxide, pellet banding
3F9N05	700	719	ZIRLO, heat-treated	56	Oxide thickness and hydride distribution
3F9N05	1425	1444	ZIRLO, heat-treated	59	Oxide thickness and hydride distribution
3F9N05	2300	2329	ZIRLO, heat-treated	57	Oxide thickness and hydride distribution
6U3K09	3506	3525	ZIRLO	42	CIRFT correlating data
F35P17	2735	2754	Zirc-4, heat treated	66	Oxide thickness, spalling oxide, pellet banding
F35P17	3050	3069	Zirc-4, heat treated	65	Peak oxide thickness, spalling oxide, pellet banding
F35P17	2383	2402	Zirc-4, heat treated	66	Oxide thickness, spalling oxide, pellet banding

E-4.1 Test Protocol, Equipment Verification, Data Processing Approach, and Measurement Uncertainty

Tests at LAMDA were performed at RT using the Buehler Wilson VH3100 Microhardness (Figure E-20) tester. The tester has both Vickers and Knoop indentation capability with a maximum load capacity of 10 kg. All tests in this report were completed using a Vickers indenter.

Figure E-20. LAMDA laboratory's Buehler Wilson VH3100 Microhardness Tester.

Prior to microhardness examination of the sample, the equipment was tested using a Sun-Tec certified[b] calibrated sample having a known Vickers hardness (HV) value. The surface of the calibrated sample was cleaned using isopropanol alcohol to remove any residue on the surface. Then, six indents were applied using forces of 0.1, 0.3 and 0.5 kg*f* (six indents in total), and were held for ~10 and 15 s, respectively. Figure E-21 shows a series of Vickers indent shapes on the sample surface that were produced by the indenter tip and were captured using a ×40 lens. As illustrated by Figure E-21, a valid indent shape is uniform such that the indent edges are straight and the diagonal lengths (shown as d_1 and d_2 in the figure) are almost identical, indicating a uniform pressure distribution under the indenter.

The Vickers hardness indent has a form of a pyramid shape with a square base that has an angle of α=136 degrees. The HV number is calculated as:

$$HV = \frac{F}{A} = \frac{2F\sin\left(\frac{136^o}{2}\right)}{d^2} \sim \frac{1.8544F}{d^2} \quad \text{(E-9)}$$

Where *F* is in kilogram-force (kg*f*), *A* is the area of the indention, and *d* is the average length of the diagonals (i.e., $d=(d_1+d_2)/2$) left by the indenter in millimeters.

[b] The calibration standard was manufactured in accordance with ASTM E92-17 and ISO/IEC 17025 on 05/10/21.

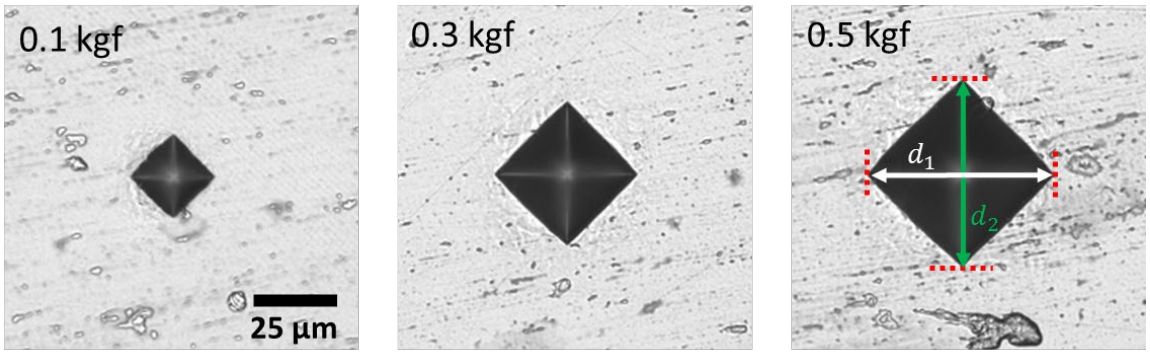

Figure E-21. The shape of indents left on the calibrated sample surface after applying 0.1, 0.3 and 0.5 kg force using ×40 lens. The scratches on the sample surface likely resulted from surface polishing. The lengths of the diagonals left by the indenter were measured as d_1 and d_2 and averaged.

The main source of error in the HV number (ΔHV) in Eq. (E-9) is the error associated with measuring the diagonal lengths (Δd). For a given load force, the relationship between Δd and ΔHV can be determined through the error propagation, where $\frac{\Delta HV}{HV}$ can be expressed using the partial derivative of Eq. (E-9):

$$\frac{\Delta(HV)}{HV} = \frac{\partial HV}{\partial d}\frac{\Delta d}{HV} = \frac{-2C}{d^3}\frac{\Delta d}{Cd^{-2}} \quad \text{, and} \tag{E-10}$$

$$\frac{\Delta(HV)}{HV} = -2\frac{\Delta d}{d} \tag{E-11}$$

In other words, Eq. E-11 indicates a 1% error in diagonal length measurement results in a 2% error in HV. Several factors can contribute to Δd, such as:

1) variations in measurements among different operators who perform the test,
2) variations in objective lenses used for diagonal length measurements, and
3) error attributed to the method itself when creating an indentation.

In the case of the sister rod data, the same person performed all tests to date. When data from the IFEL equipment are available, comparisons between the results obtained with the LAMDA and IFEL equipment will be examined for biases.

A ×60 objective lens is used for measurements at LAMDA, and for this lens, the error for each diagonal was taken to be ±4 pixels (i.e., 2 pixels at each corner). Image resolution at this magnification is 576 × 480 pixels, and 1 pixel was calculated to be ~ 0.24 µm.

Prior to conducting microhardness tests, indents were made on a calibration standard and were measured for verification of the LAMDA equipment. Table E-5. summarizes the microhardness test parameters and the corresponding HV numbers (HV_m) determined from Eq. (E-9) for the calibration standard. The measured HV of the calibration standard was consistent with the HV provided by the manufacturer (HV_{ref}) and were within the expected measurement error.

Table E-5. Standard sample hardness measurement results using VH3100 Microhardness tester compared with the reference hardness measurements.

Indent #	Load (kgf)	Hold time (s)	Measured hardness (HVm)	Certified hardness (HVref)*	% Relative error $\left\|\frac{HV_m - HV_{ref}}{HV_{ref}}\right\|$
1	0.1	10	303 ± 10	301 ± 4.8	2.3
2	0.3	10	301 ± 24		2.0
3	0.5	10	299 ± 14		0.3
4	0.1	15	295 ± 10		2.0
5	0.3	15	294 ± 10		2.3
6	0.5	15	298 ± 13		1.0

* HV_{ref} is given as an average hardness of five different measurements (varying from 295 to 307 HV) conducted at RT using 0.5 kg-force. The estimated uncertainty in the certified hardness was calculated by the provider within 95% confidence level.

For the cladding measurements, microhardness indents will be made in each quadrant using a standardized force and spacing, starting from the cladding's inner diameter (ID) and moving radially toward OD, with each indention held for 10 s. According to the ASTM E92-17, the minimum spacing between each individual indent and between an indentation and the edge of the sample should be 2.5 × the indent's diagonal length, as illustrated in Figure E-22, to avoid an inaccurate measurement.

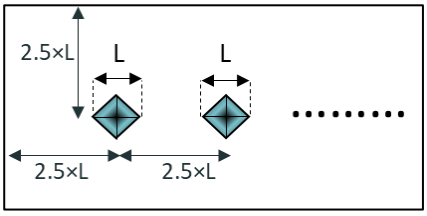

Figure E-22. Illustration of minimum recommended spacing for Vickers indentations and the measured diagonal length, L.

Considering this guideline, the maximum number (N) of indents that can fit in each quadrant of the fuel cladding can be estimated using Eq. (E-12):

$$N = \frac{t_{clad}}{2.5L} - 1, \tag{E-12}$$

where t_{clad} is the cladding thickness, and L is the average diagonal length.

Given the cladding thickness of the sister rod specimens, Eq. E-12 was used to estimate the number of indents (N) possible. A few individual indents were arbitrarily created on a sister rod sample using different test forces ranging from 0.1 to 1 kgf. The diagonal lengths (L) of the resultant indents were measured; some of these indents are shown in Figure E-23, with the corresponding test forces indicated. The average diagonal length of each indent and the corresponding HV value was calculated and plotted with respect to the applied test force as shown in Figure E-25. Figure E-24 shows an almost linear relationship between the test force and the average indent size. The corresponding HV initially shows a modest increase from HV 257 ± 9 at 0.1 kgf to HV 263 ± 6 at 0.3 kgf. However, when a test force of 1 kgf was applied, a pronounced reduction in HV was found. It is possible that the plastic zone created by the indent tip at this test force extended beyond the specimen and started to sample the epoxy mounting media, causing the

reduction. Therefore, to reduce the uncertainty in the microhardness measurements and to increase the number of indents that could be applied, a test force of 0.1 kgf was selected for application in these tests. Considering the cladding thickness and the indent size at this test force, 7 indents can be made across the cladding thickness, starting from the cladding ID and moving radially toward OD, with each indention held for 10 s.

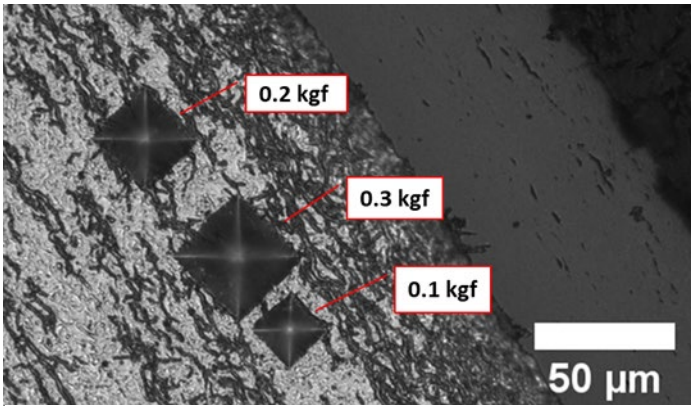

Figure E-23. Micrograph comparing microhardness indents formed using different loads.

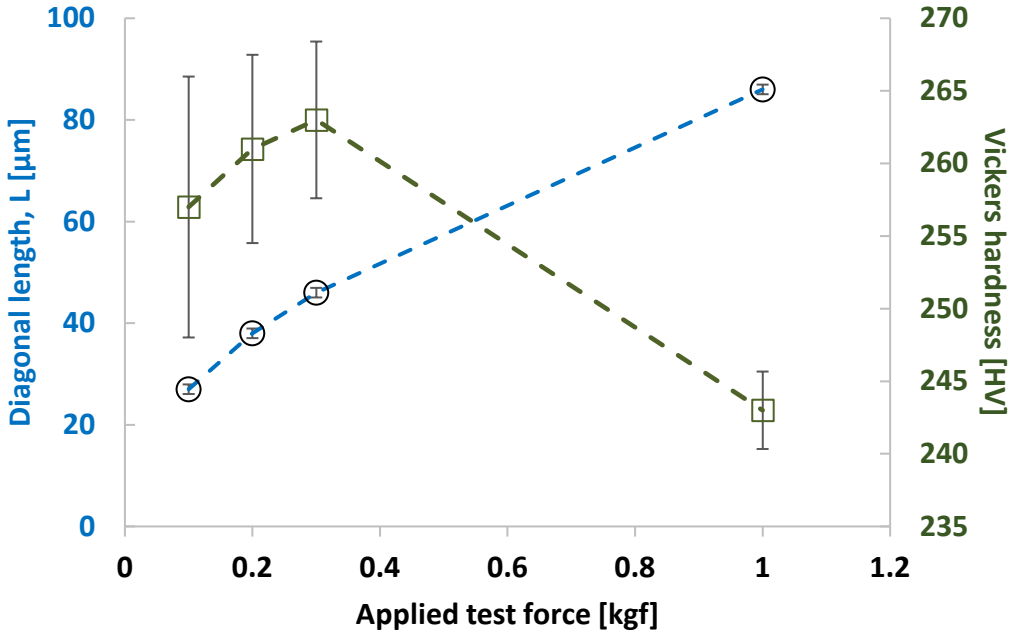

Figure E-24. Measured indent's diagonal length (L) and HV as a function of applied test force in kilogram-force.

Use of the lighter 0.1 kg load for the intents results in smaller indents, as shown in Figure E-23. Per the applicable ASTM standards, if the indents produced in the test are are less than 20 µm the testing is classified as light force testing. However, the considerations for light force testing are mainly applied for Knoop-type hardness testing, because of the pyramidal diagonal inherent in the geometry of the Knoop indenter tip. ASTM strongly suggests to avoiding light load forces for Knoop indention. For Vickers hardness testing, the indent geometry is constant with load, and increasing/decreasing the indention load only changes the size of the indent, not its geometry, and visibility of the smaller indention is generally the only concern related to load selection for Vickers hardness testing. For these tests, both the indent size and the selected load are higher than the ASTM-recommended thresholds for Vickers hardness testing and are considered acceptable.

E-4.2 Vickers Hardness Data

Microhardness tests were performed on a defueled polished sample prepared from segment F35P17-2735-2754 (heat-treated Zirc-4 cladding) [E-7]. After the equipment setup was verified with the calibration standard, the defueled cladding sample was mounted on the microhardness tester. An overview optical microscopy image of the sample prior to the microhardness test is shown in Figure E-25, in which the epoxy, cladding, oxide layer, and spalled oxide locations are indicated with arrows. The rectangles in Figure E-25 highlight the locations where the microhardness test was conducted. Four of these locations are perpendicular to each other (Quads A, B, C and D). The fifth location, Quad-AB, is the region where spalled oxide was observed.

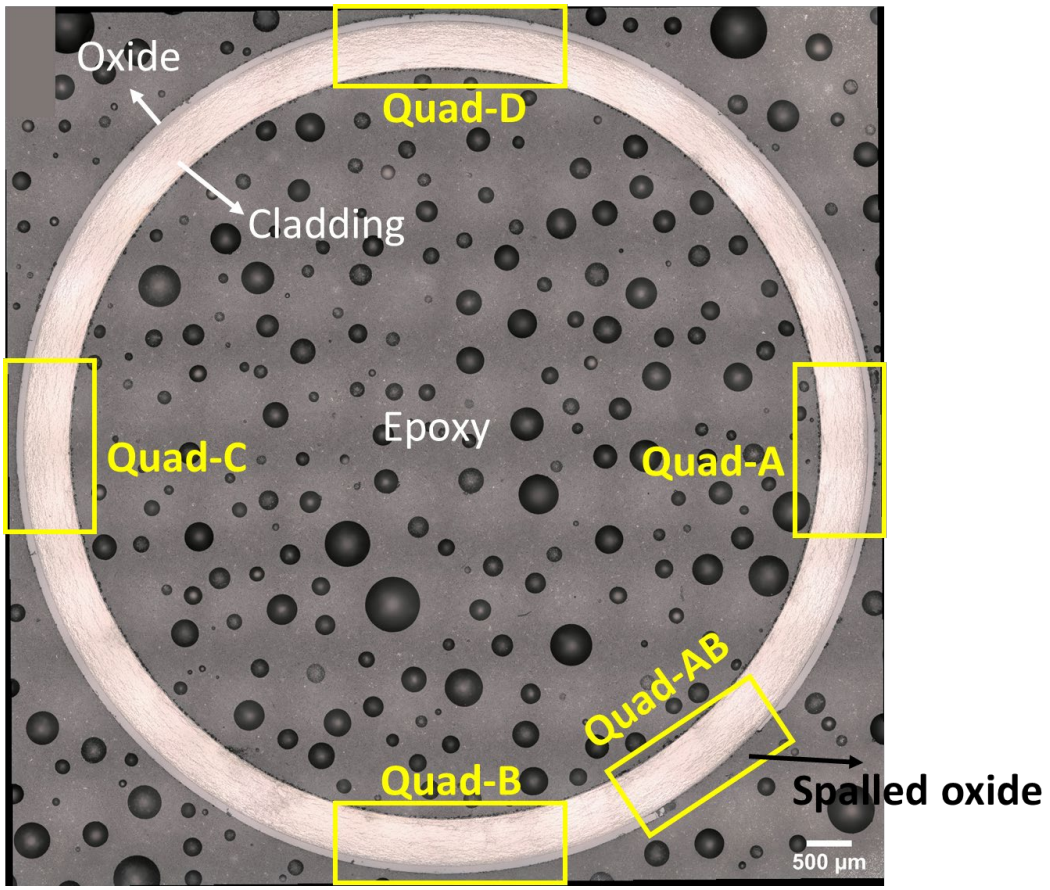

Figure E-25. Optical microscopy image of defueled F35P17-2735-2754 sample prior to microhardness test with test locations indicated.

Figure E-26 provides an example of microhardness indents across the width of the cladding for Quad-A. An indention was also made in the waterside oxide layer. Because the oxide layer is harder than the cladding, the indent on the oxide is smaller than the indents on the metal.

For best results, ASTM suggests not etching the samples if possible before making indentation. This is mainly because deeply etched surfaces can obscure the edge of the indentations and may cause difficulties in achieving an accurate measurement of the size of the indentation. In our case, the indent shapes are clearly visible even in the region where there is high hydride density.

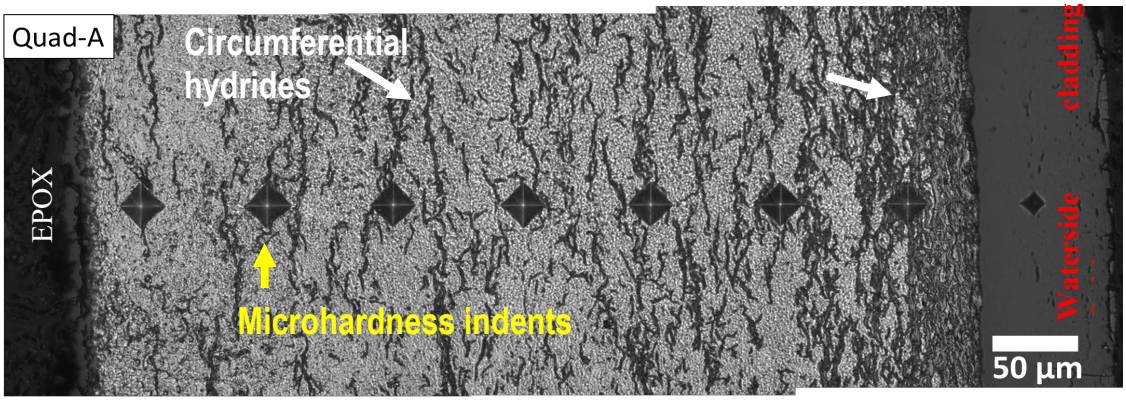

Figure E-26. Microhardness indents formed on cladding specimen F35P17-2735-2754 using 0.1 kg*f* (×40 lens). The waterside oxide-clad interface is highlighted with the blue dashed line

Figure E-27 shows the indents on all quadrants of the sample. The cladding wall thickness and oxide thickness measured from these micrographs are also provided in Figure E-27, and they are consistent with previous NDEs and metallography (MET) measurements reported by Montgomery et al. [E-7] and in other sections of this report.

The measured HV and the average for each quadrant are provided in Table E-6, and are plotted in Figure E-28 as a function of radial distance from the clad ID. Each indentation includes varying numbers of hydrides, which are expected to be harder than the metal matrix. This particular specimen includes a high density of hydrides across the entire cladding wall, with an even higher density hydride rim at the waterside oxide layer interface. Figure E-28 shows small variations in the quadrant data that are within measurement uncertainty. Scattering in the dataset is likely caused by the variations in local hydride morphologies. The hydrides are visible in Figure E-26 and Figure E-27 as dark linear regions within the metal matrix because the section was etched for imaging. In some cases, the darker appearance of the hydrides makes it difficult to locate the diagonal corners for the HV measurement when they coincide with a hydride precipitate. This dark appearance contributes to a slightly higher measurement uncertainty for this specimen.

The measured HV in each quadrant of the cladding was consistent with each other, and it was uniform up to a distance of ~400 µm from the cladding ID, beyond which the hydride density increased, resulting in an increment in the measured HV. Figure E-28 indicates the trend of increasing HV with radius, with the waterside cladding locations measuring ~25 HV harder than the ID locations. This result is consistent with previous measurements [E-8]. The HV value for Quad-AB, where spalling oxide was observed, is similar to the HV values obtained for the other quadrants, where a uniform oxide film is present. The observed trend of increased hardness near the clad OD was also found in this quadrant and is consistent with other quadrants. The maximum quadrant average HV for the HBU Zirc-4 specimen tested was 290 ± 8 HV.

Further microhardness tests are planned in FY22.

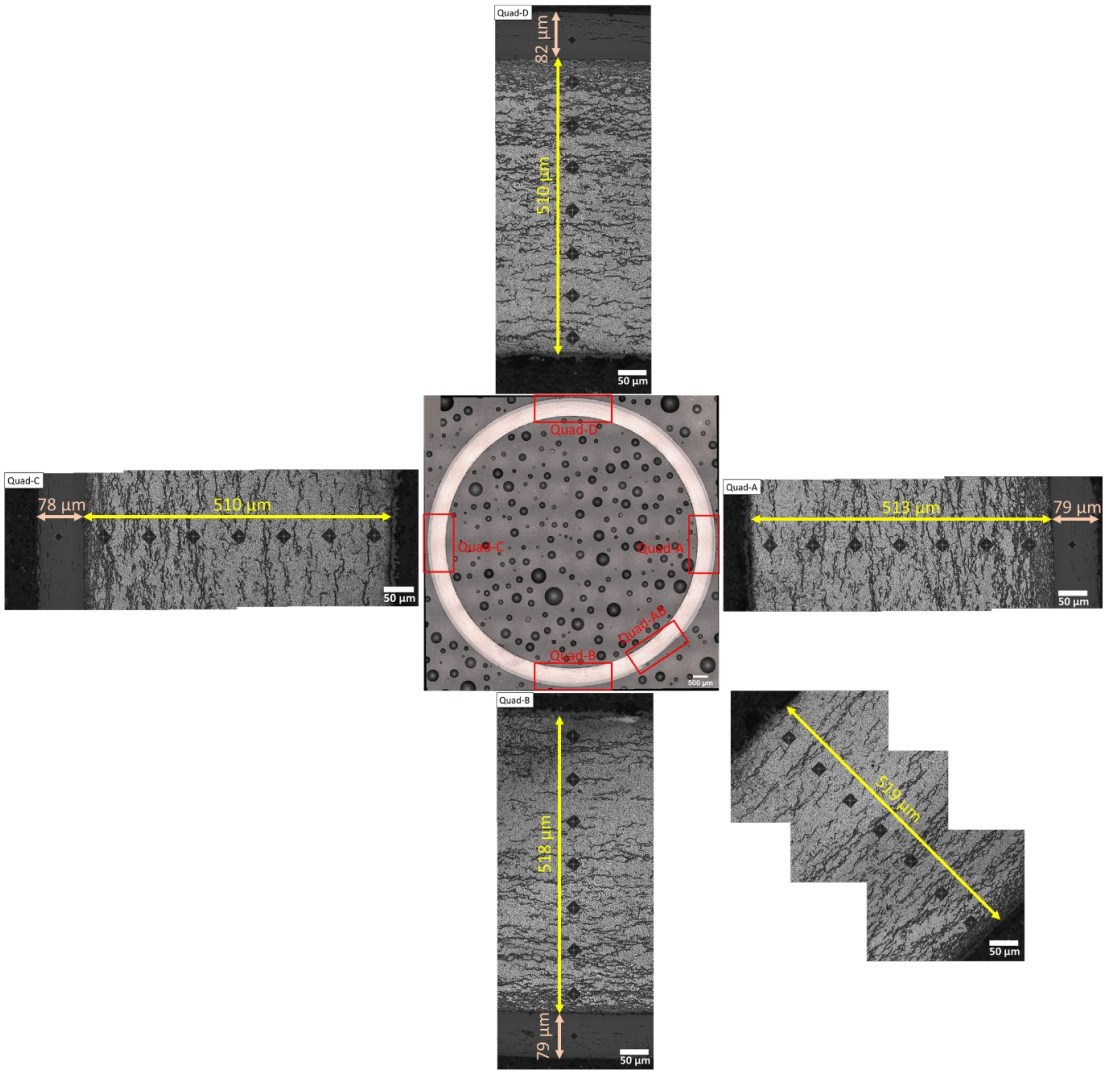

Figure E-27. Micrographs showing the microhardness indents in each highlighted region (×20 lens). The cladding wall thickness and the oxide thickness are indicated on the micrographs.

Table E-6. Microhardness summary table for F35P17-2735-2754.

	Indent #	Location from clad ID (μm)	HV
Quad-A	1	34	252 ± 9
	2	108	256 ± 9
	3	184	259 ± 9
	4	259	267 ± 10
	5	334	272 ± 10
	6	409	279 ± 10
	7	484	289 ± 11
	8 (Oxide)	559	930 ± 62
Quad-B	1	37	278 ± 10
	2	112	262 ± 9
	3	187	271 ± 10
	4	262	269 ± 10
	5	337	258 ± 9
	6	412	271 ± 10
	7	487	295 ± 11
	8 (Oxide)	554	929 ± 62
Quad-C	1	29	251 ± 9
	2	104	255 ± 9
	3	179	257 ± 9
	4	254	270 ±10
	5	329	270 ± 10
	6	404	275 ± 10
	7	479	279 ± 10
	8 (Oxide)	554	978 ± 67
Quad-D	1	27	263 ± 10
	2	102	263 ± 9
	3	177	270 ± 10
	4	252	271 ± 10
	5	327	273 ± 9
	6	402	284 ± 10
	7	477	298 ± 11
	8 (Oxide)	552	952 ± 64
Quad-AB	1	40	261 ± 9
	2	115	263 ± 9
	3	190	265 ± 10
	4	265	269 ± 9
	5	340	276 ± 10
	6	415	283 ± 10
	7	490	297 ± 11
	8	N/A (spalled)	N/A
Maximum (excluding oxide)		Quad D, 477	298 ± 11
Minimum (excluding oxide)		Quad C, 29	251 ± 9
Average (excluding oxide)		N/A	271 ± 11
Maximum (oxide)		Quad C	978 ± 67
Minimum (oxide)		Quad B	929 ± 62
Average (oxide)		N/A	947 ± 67

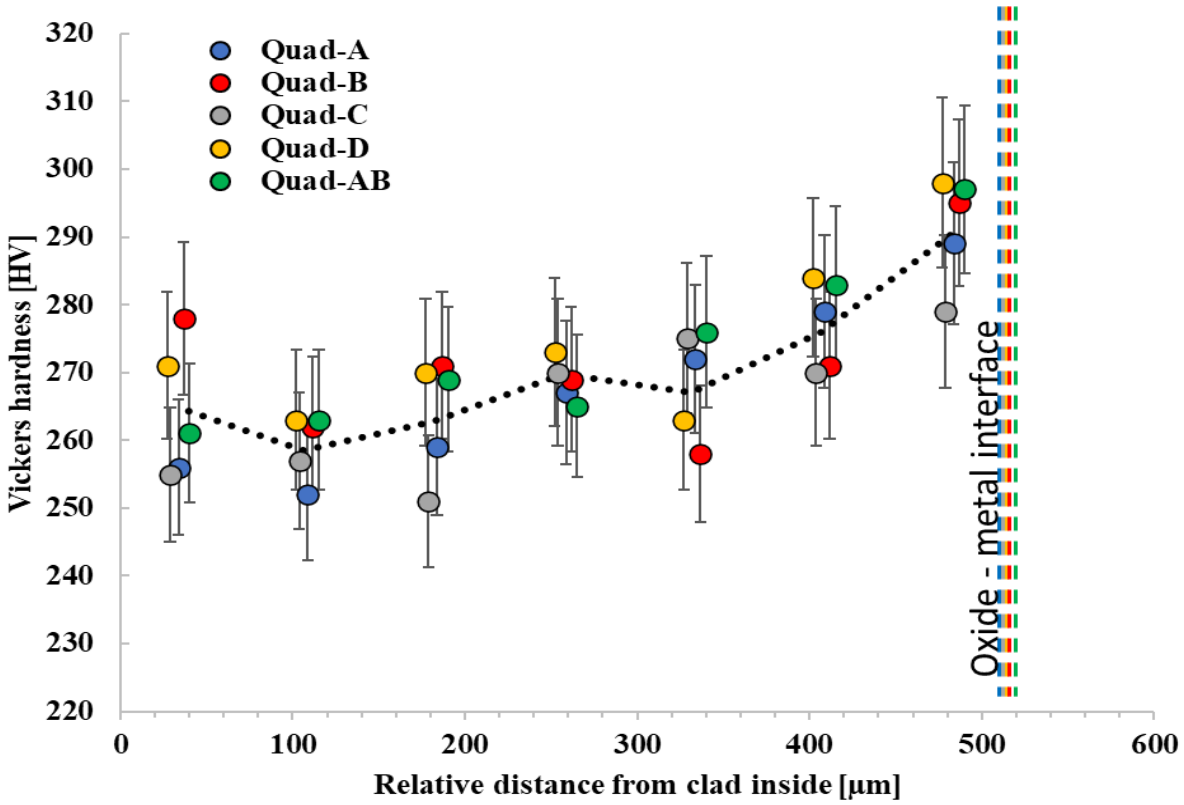

Figure E-28. HV and average HV (dotted line) for each quadrant from ID to OD for specimen F35P17-2735-2754 at RT using an indent of 0.1 kgf.

E-5. Ring Compression Tests

A significant body of data on cladding hydride reorientation and associated effects on cladding ductility was developed by Argonne National Laboratory (Argonne) over the last decade, with the most recent summary of results documented by Billone et al. in 2019 [E-9]. Several baseline and heat-treated sister rod specimens were shipped to Argonne for cladding ring compression tests (RCTs), and several specimens have been tested [E-9, E-10].

ORNL's data provide supplementary information on the load-bearing capability of intact fuel rods (cladding and pellets). Similar to the RCT of cladding specimens, the fueled rod segment is loaded across its diameter, and the load to specimen failure is measured.

E-5.1 Test Procedure and Data Processing

E-5.1.1 Test Protocol

Instrument and software testing equipment description:

Load frame	Instron 5967
Bend fixture capacity:	30 kN
Voltage:	110/220 V
Software:	Bluehill-3
Furnace:	CP122117 Environmental Chamber and Control Unit
Furnace max temperature:	≤400°C
Scale:	Ohaus Scout NV1201

The RCTs use a pair of 2 in. diameter flat steel compression platens rated to 30 kN. Each specimen is stored separately, and only one specimen is removed from its labeled storage container at a time.

The test specimen is centered on the lower platen using an elastomeric O-ring (RT tests) or a carriage washer (200°C tests). The upper platen is lowered to a position approximately 3 mm above the specimen.

If the test is at temperature, then the furnace door is closed, and heating is initiated. During heating, the upper RCT platen is raised as needed to avoid specimen preload due to thermal expansion of the system.

Once the system is at the specified temperature, the upper RCT platen is lowered to contact the test specimen, as indicated by an increase in load. Care is taken to keep the amount of initial loading small.

The test system is then zeroed, and the test is initiated. All tests are run using a fixed displacement speed of 0.0125 mm/s. The test proceeds until the specimen is fractured.

Following fracture, the specimen, as defined by the fueled pieces within the cladding, is weighed. Any loose particles are weighed. The post-test specimen is placed in a labeled capsule and returned to storage.

E-5.1.2 Test Specimen

The RCT specimens were rough cut to 90 mm. The 90 mm specimens were sub-cut to test specimens that were ~25 mm long for RCT. Each specimen should contain two full pellets. The specimen was sized to avoid pellet loss from the unsupported ends that could invalidate the results, and the 25 mm length was successful for that purpose.

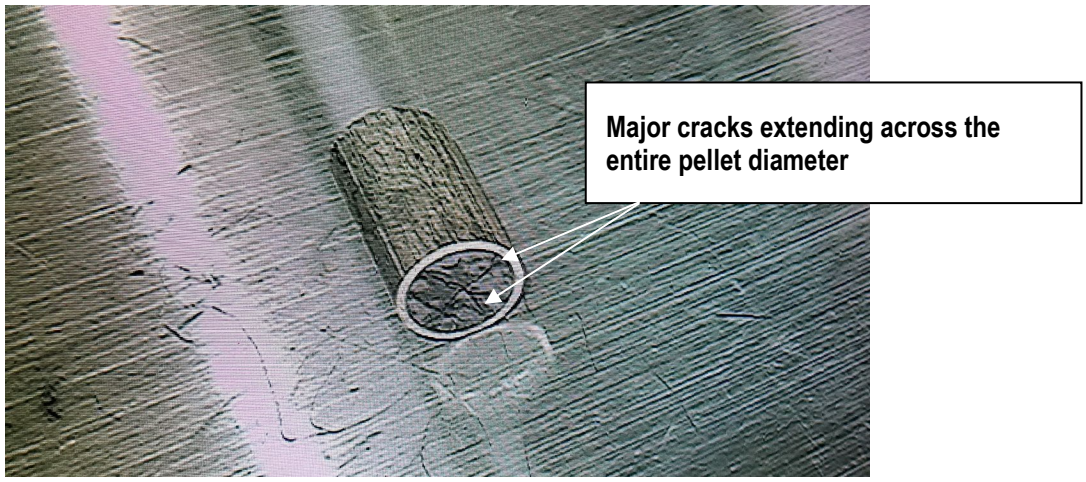

Figure E-29. Typical test specimen.

E-5.1.3 Data Reduction

A typical load vs. a displacement curve, as corrected for machine compliance, is shown in Figure E-30. The specimen takes on load, sometimes with a small drop as the operationally cracked pellets rearrange slightly, until the cladding fractures and the specimen splits open. If the test continues, then the section is crushed and eventually begins to take on load again as the pellet fragments are engaged in the load path. For the purposes of this study, only the peak load achieved is reported.

As discussed in Section E-2.1.2, the load vs. crosshead extension data necessarily includes the machine's compliance. For RCT, the machine compliance is measured by testing an empty pressing die (more than ten times the load frame capacity) using the RCT setup. The corrected displacement is calculated by subtracting the displacement reported in the machine compliance test from the displacement reported in the test of each sister rod specimen.

Unlike the 4PB specimens, the RCT specimens fracture at more than half of the load frame's limit, and the correction made to the RCT displacement is significant. Figure E-31 plots the RCT compliance used in correcting the RCT specimen data.

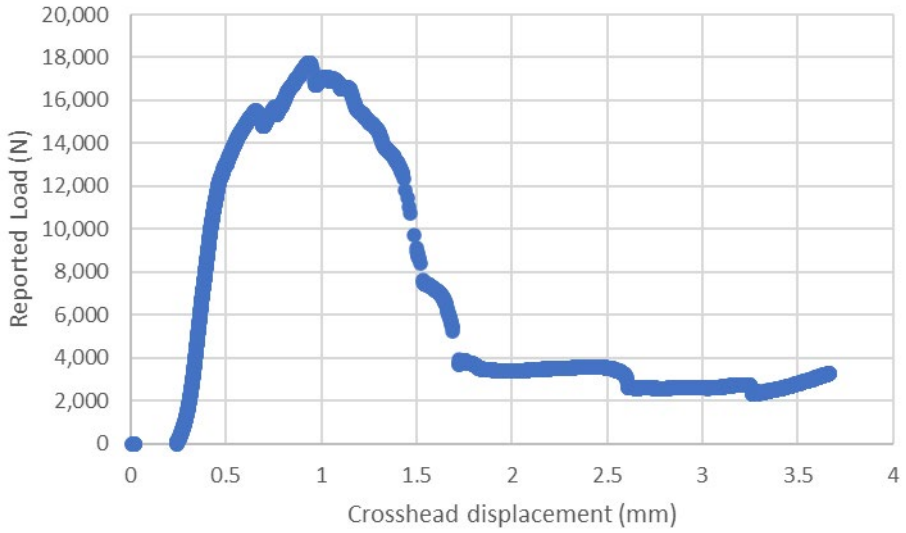

Figure E-30. Typical load vs. crosshead displacement for fueled RCT.

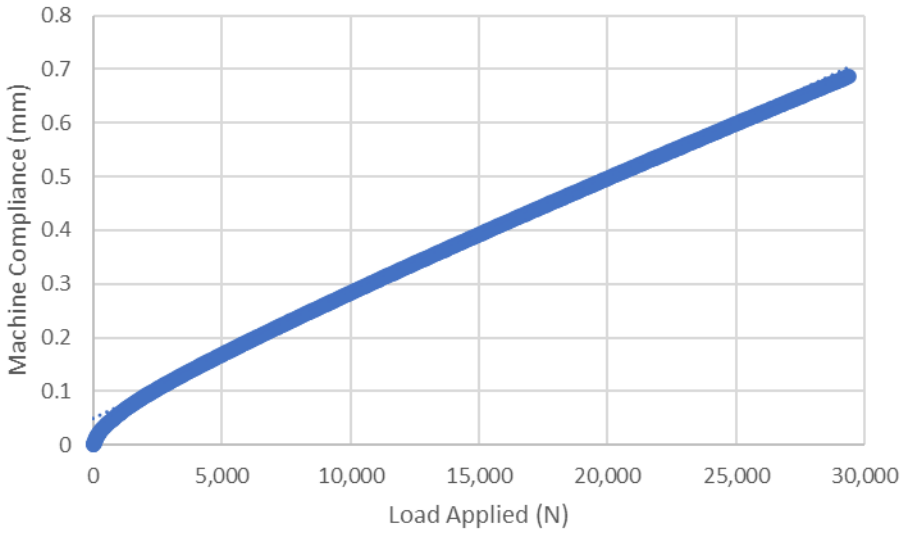

Figure E-31. Measured load frame compliance used to correct RCT data.

E-5.2 Peak Load Data

Table E-7 lists the peak loads recorded for the specimens tested in RCT. The average load-bearing capability of the segments in transverse compression is 16,415 N (3,690 lb_f). As shown in Figure E-32, there is no trend with specimen average burnup, and there is no appreciable difference in the maximum load from RT to 200°C. Cladding type also does not greatly influence the load-bearing capability, and there is no difference related to the heat-treatment applied to some of the rods, as shown in Figure E-33.

Table E-7. RCT peak load data.

Sample ID#	Test temperature (°C)	Cell temperature (°C)	Cladding alloy	Heat-treatment	Estimated specimen burnup (GWd/MTU)	Peak load (N)	Peak load (lb_f)
30AD05-2320-2345	25.2	25.2	M5	---	59	17,985	4,043
30AD05-3150-3175	25.3	25.3	M5	---	56	17,000[a]	3,822[a]
30AE14-2585-2610	25.9	25.9	M5	FHT	60	17,632	3,964
30AE14-3418-3443	25.9	25.9	M5	FHT	47	19,510	4,386
3D8E14-2322-2347	25.1	25.1	ZIRLO	---	64	15,788	3,549
3D8E14-3116-3141	25.1	25.1	ZIRLO	---	60	17,210	3,869
3D8E14-2347-2372	200	26.2	ZIRLO	---	64	17,752	3,991
3F9N05 -2482-2507	25.6	25.6	ZIRLO	FHT	59	17,444	3,921
3F9N05-3350-3375	25.6	25.6	ZIRLO	FHT	50	17,049	3,833
3F9N05-3375-3400	200	25.8	ZIRLO	FHT	50	18,683	4,200
3A1F05 -3124-3149	24.8	24.8	LT Zirc-4	---	52	12,303	2,766
3A1F05-2645-2670	24.9	24.9	LT Zirc-4	---	55	16,232	3,649
3A1F05-2670-2695	200	25.8	LT Zirc-4	---	55	12,384	2,784
F35P17-2645-2670	25.7	25.7	Zirc-4	FHT	51	12,476	2,805
F35P17-2960-2985	25.7	25.7	Zirc-4	FHT	50	12,961	2,914
F35P17-2670-2695[b]	200	25	Zirc-4	FHT	51	15,915	3,578
F35P17-2985-3010[c]	200	25.3	Zirc-4	FHT	50	12,500[a]	2,810[a]
					Maximum	20,732	4,661
					Minimum	12,303	2,766
					Average	16,415	3,690

a. The data file was not saved for this test. The value is from the estimate recorded in the laboratory notebook.
b. A major pellet crack as aligned with the loading direction.
c. A major pellet crack as aligned perpendicular to the loading direction.

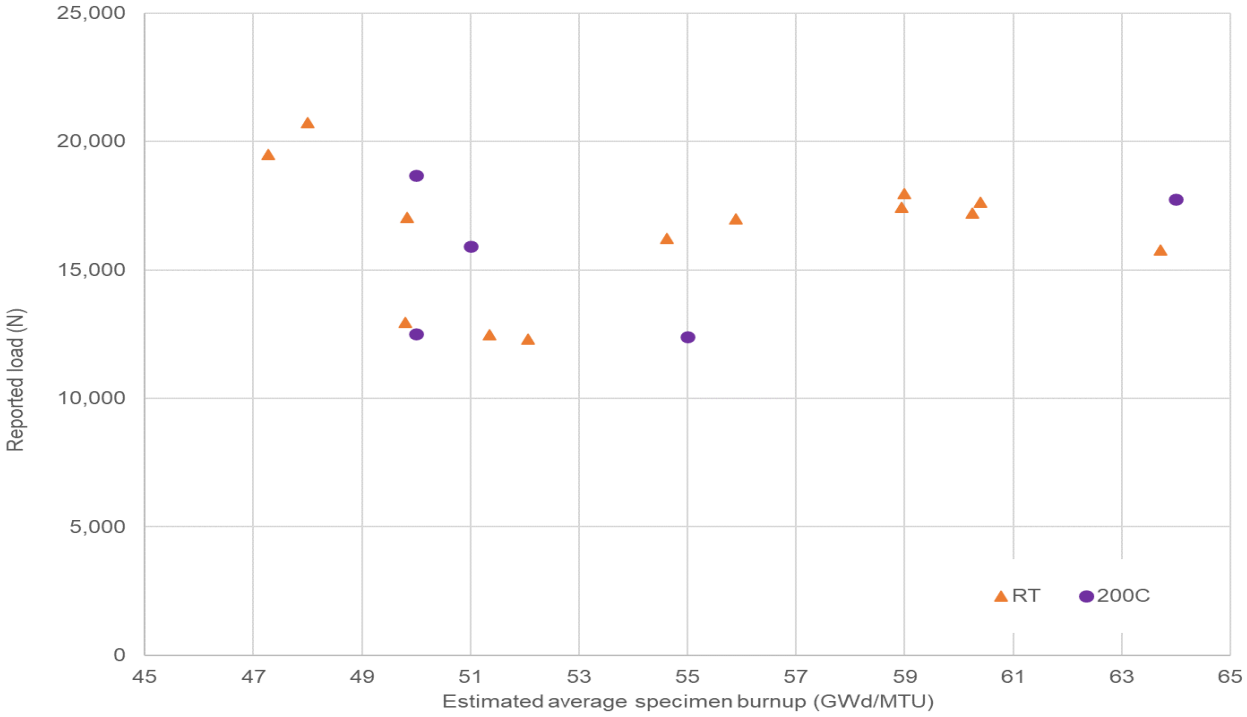

Figure E-32. Maximum RCT load vs. estimated average specimen burnup at RT and 200°C RCT.

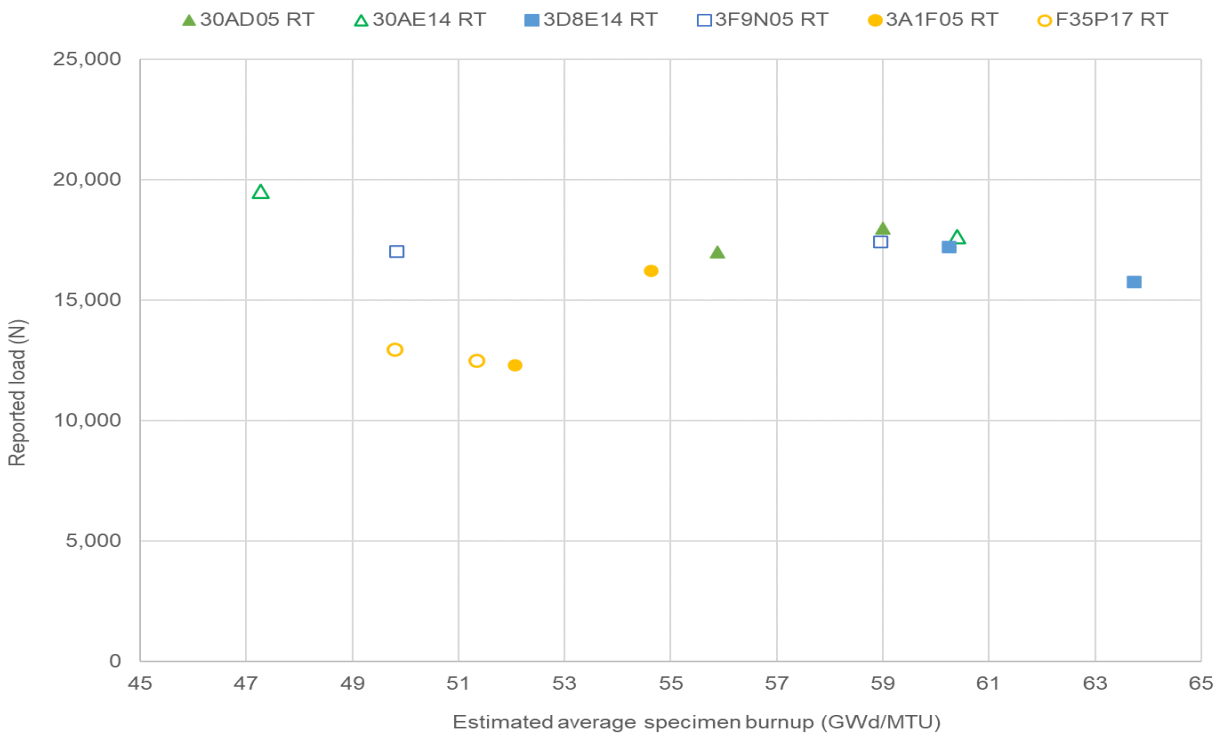

Figure E-33. Maximum RCT load vs. average specimen burnup at RT for baseline and FHT specimens.

The results for a ZIRLO-clad fueled RCT are compared with results from a defueled ZIRLO RCT [E-9] in Figure E-34. The fueled cladding carries about eight times the load of the defueled cladding, but it fractures at a much lower displacement because it is constrained by the pellet. The defueled RCT's predictably fracture at the 3 and 9 o'clock cladding positions [E-9,E-10], whereas the fueled RCTs fracture at a major pellet crack.

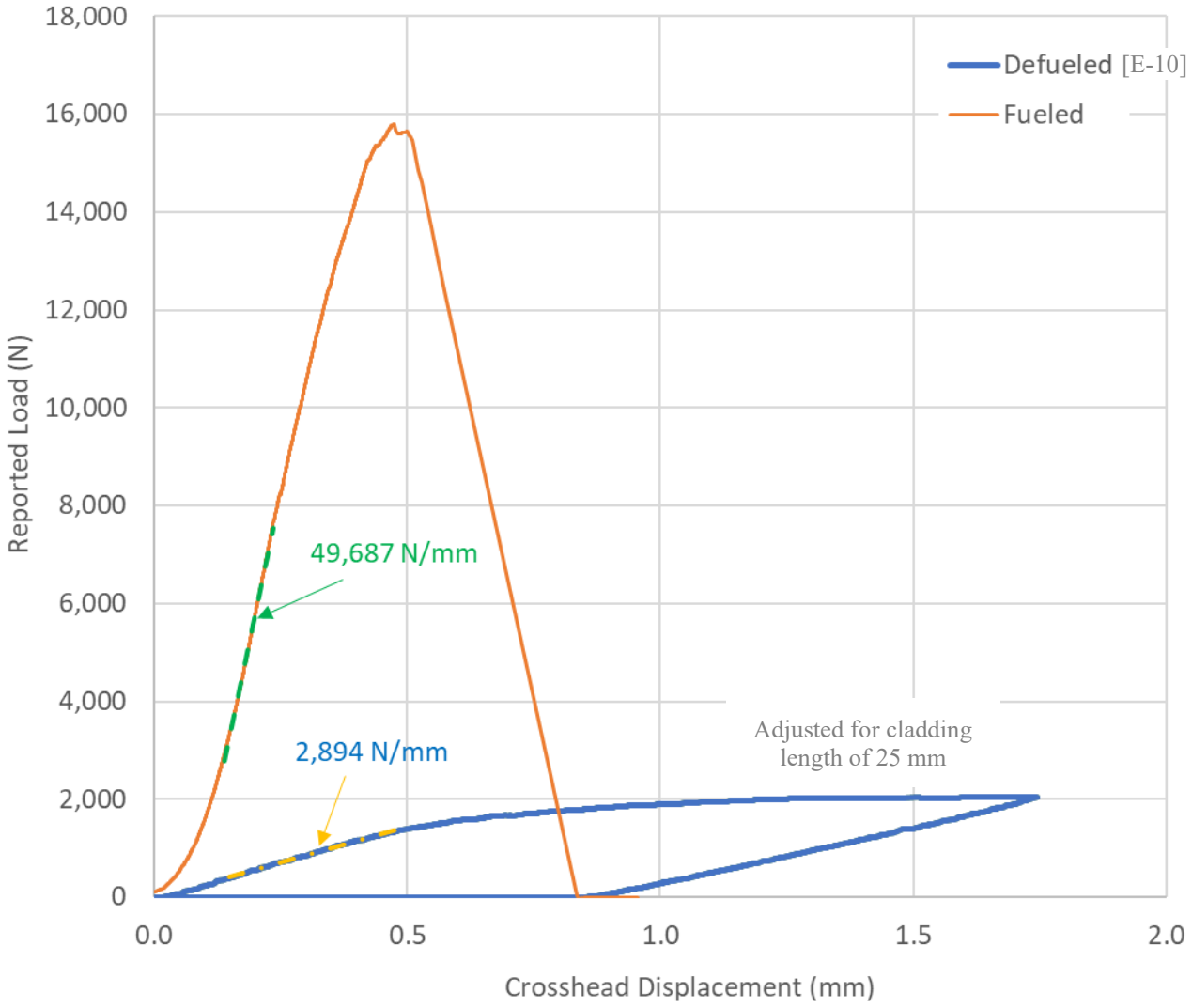

Figure E-34. Comparison of load vs. crosshead displacement for a ZIRLO sister rod specimen, fueled and defueled.

E-5.3 Typical Fracture Observed

The specimens typically carried load until at least one cladding fracture developed. As shown in Figure E-35, specimens frequently broke into two equal halves. As the tests progressed, it became clear that fracture typically occurred at the location of one of the major diametrical pellet cracks, as illustrated in Figure E-36. Usually, there were two major cracks (defined as *full-diameter cracks*) visible at the end of the specimen. Two specimens from F35P17 were tested with the major crack aligned along the loading path and perpendicular to the loading path. There was a difference in the results for those two samples, but unfortunately, the data were not recorded within the software for one of the tests, and only the notation on peak load in the laboratory notebook is available, which is not exact.

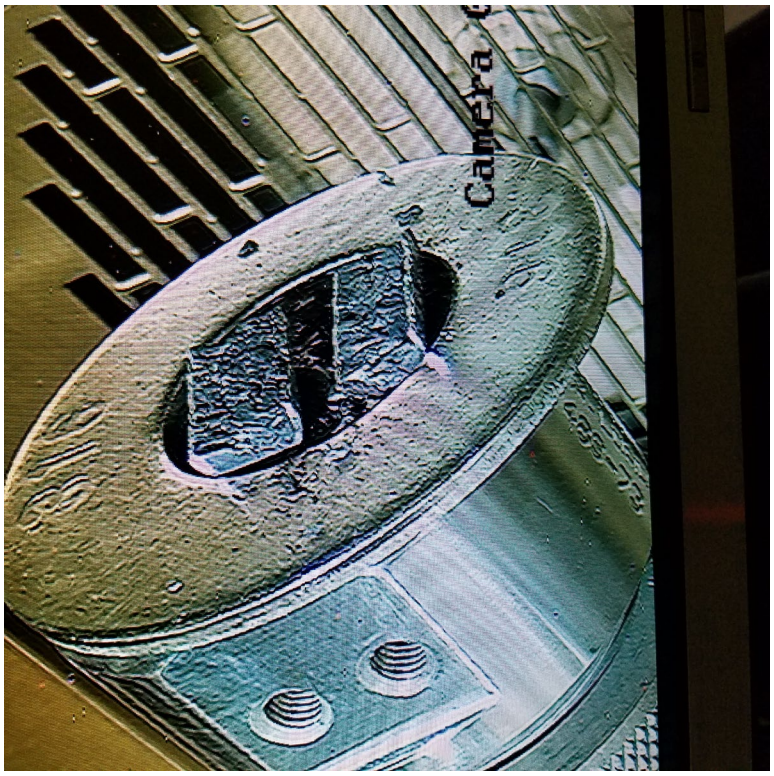

Figure E-35. Typical post-RCT appearance.

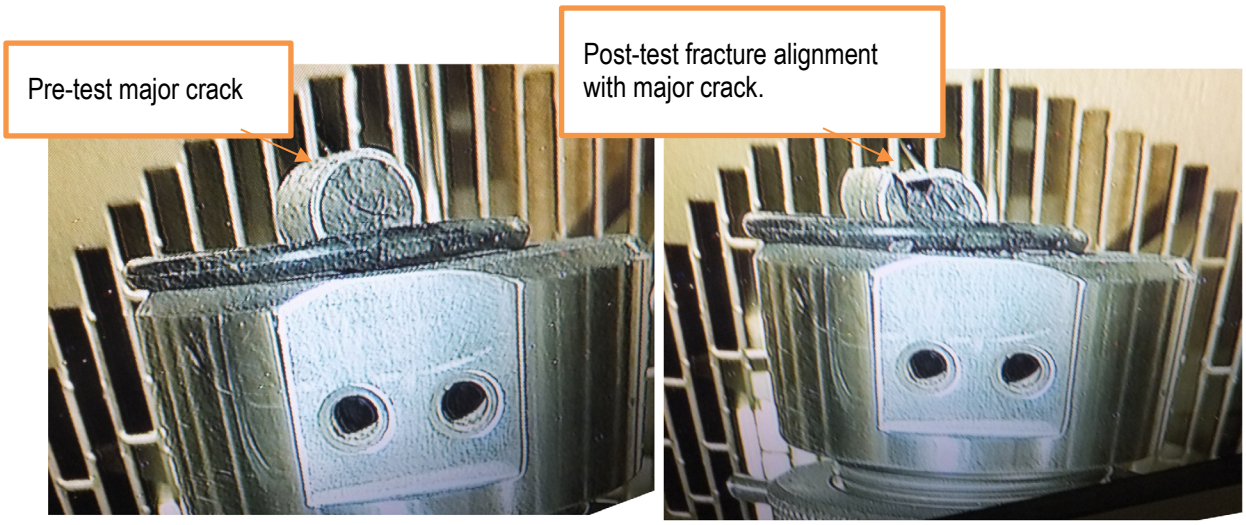

Figure E-36. RCT fracture path along major pellet crack.

E-6. Burst Tests

In FY21, ORNL investigated its existing equipment for use in burst testing fueled specimens. One goal of the burst tests is to capture aerosols released in the burst. To achieve this goal, a gas must be used to pressurize the test specimen, and the test must be conducted at RT. Given these criteria, the existing equipment is not capable of reaching the necessary pressure.

ORNL is collaborating with PNNL to design a new system to pressurize segments for burst that is similar to their system for cladding burst; however, the system at ORNL will use a gas. With a basic design in hand, ORNL plans to acquire the necessary equipment in FY22 for testing near the end of FY22.

References

[E-1.] *High Burnup Dry Storage Cask Research and Development Project: Final Test Plan*, Contract no. DE-NE-0000593, Electric Power Research Institute, Palo Alto, California (2014).

[E-2.] S. Saltzstein et al., *Visualization of the High Burnup Spent Fuel Rod Phase 1 Test Plan*, SAND2018-8042-O (2018).

[E-3.] R. A. Montgomery et al., *Post-Irradiation Examination Plan for High Burnup Demonstration Project Sister Rods*, SFWD-SFWST-2017-000090 ORNL/SR-2016/708, Oak Ridge National Laboratory, Oak Ridge, Tennessee, 2016.

[E-4.] ASTM International (2018). ASTM C1161 – 18: Standard Test Methods for Flexural Strength of Advanced Ceramics at Ambient Temperature. West Conshohocken, PA: American Society for Testing and Materials.

[E-5.] ASTM International (2015). ASTM D7264/D7264M – 15: Standard Test Methods for Flexural Properties of Polymer Matrix Composite Materials. West Conshohocken, PA: American Society for Testing and Materials.

[E-6.] ASTM International (2016). ASTM E8/E8M – 16a: Standard Test Methods for Tension Testing of Metallic Materials. West Conshohocken, PA: American Society for Testing and Materials.

[E-7.] R. A. Montgomery et al., *Sister Rod Nondestructive Examination Final Report*, SFWD-SFWST-2017-000003 Rev. 1 (M2SF-17OR010201021) / ORNL/SPR-2017/484 Rev. 1 (ORNL/SPR-2018/801), Oak Ridge National Laboratory, Oak Ridge, Tennessee, 2019.

[E-8.] R. W. Shimskey et al., *FY2020 Sibling Pin Testing Results,* M2SF-21PN010201055 / PNNL-31036, Pacific Northwest National Laboratory, Richland, Washington, 2020

[E-9.] M. C. Billone, *Ductility of High-Burnup-Fuel ZIRLO™ following Drying and Storage*, ANL-19/14, M2SF-19AN010201011 Rev. 3, Argonne National Laboratory, June 30, 2019.

[E-10.] M.C. Billone, T.A. Burtseva, Y. Chen and Z. Han, Ductility of M5® and ZIRLO® Sibling Pin Cladding, M2SF-20AN010201012/ANL-20/47 (2020).